A novel mutation in SPART gene causes a severe neurodevelopmental delay due to mitochondrial dysfunction with Complex I impairments and altered pyruvate metabolism

Running title: SPART and mitochondria in Troyer syndrome

Chiara Diquigiovanni[1], Christian Bergamini[2], Rebeca Diaz[3], Irene Liparulo[2], Francesca Bianco[1], Luca Masin[2], Vito Antonio Baldassarro[4], Nicola Rizzardi[2], Antonia Tranchina[1], Francesco Buscherini[1], Anita Wischmeijer[5], Tommaso Pippucci[1], Emanuela Scarano[6], Duccio Maria Cordelli[7], Romana Fato[2], Marco Seri[1], Silvia Paracchini[3], Elena Bonora[1*]

[1]Department of Medical and Surgical Sciences, DIMEC, St. Orsola-Malpighi Hospital, University of Bologna, Bologna, Italy.

[2]Department of Pharmacy and Biotechnology, FABIT, University of Bologna, Bologna, Italy.

[3]School of Medicine, University of St Andrews, St Andrews, United Kingdom.

[4]IRET Foundation, Ozzano Emilia, Bologna, Italy.

[5]Clinical Genetics Service, Department of Pediatrics, Regional Hospital of South Tyrol, Bolzano, Italy.

[6]Rare Unit Disease, Department of Pediatrics, University of Bologna, St. Orsola-Malpighi Hospital, Bologna, Italy.

[7]Child Neurology and Psychiatry Unit, University of Bologna, St. Orsola-Malpighi Hospital, Bologna, Italy.

* To Whom Correspondence should be addressed:

Dr. Elena Bonora, PhD, Department of Medical and Surgical Sciences, DIMEC, Policlinico S.Orsola-Malpighi Hospital, via Massarenti 9, 40138 Bologna, Italy. Tel: +390512088434. Fax: +390512088416. Email: elena.bonora6@unibo.it

Keywords:

Spartin, Spastic paraplegia Gene 20, mitochondrial dysfunctions, pyruvate metabolism

Abbreviation

AcCoA Acetyl-coA

ALS Amyotrophic Lateral Sclerosis

BMP Bone Morphogenic Protein

Ca^{2+} Calcium

CAT Catalase

Complex I NADH dehydrogenase

Complex I+III NADH-cytochrome c reductase activity

Complex II+III succinate-cytochrome c reductase activity

CS Citrate Synthase

DAPI 4′,6-diamidino-2-phenylindole

DB Decylbenzoquinone

DCFDA 2',7'–dichlorofluorescin diacetate

DDS Deciphering Consortium

DMEM Dulbecco’s modified Eagle’s medium

DTNB 5,5′-dithiobis-2-nitrobenzoic acid

ECM Extra-Cellular Matrix

ExAc Exome Aggregation database

FCCP carbonyl cyanide-4-(trifluoromethoxy) phenylhydrazone

GH Growth Hormone

gnomAD Genome Aggregation database

gRNA guide RNA

GRP75 Glucose-Regulated Protein 75

hESC human embryonic stem cell

hNSC human neural stem cell

hpf hours post fertilization

HPLC High Performance Liquid Chromatography

HSP Hereditary Spastic Paraplegia

IMS Inter-Membrane Space

IUGR Intra-Uterine Growth Restriction

MIM Mitochondrial Inner Membrane

MIT Microtubule Interacting and Trafficking

MOM Mitochondrial Outer Membrane

MPC Mitochondrial Pyruvate Carrier

MTG Mitotracker Green

mΔψ Mitochondrial transmembrane potential

OXPHOS oxidative phosphorylation

PDH Pyruvate Dehydrogenase

pSpCas9n(BB)-2A-GFP Cas9 from *S. pyogenes* with 2A-EGFP

pSpgRNA *S. pyogenes* Cas9 guide RNA

RIPA Radioimmunoprecipitation assay

ROH Runs Of Homozygosity

ROS reactive oxygen species

SD standard deviations

SDS-PAGE sodium dodecyl sulfate polyacrylamide electrophoresis

SEM Standard Error of Mean

SNPs Single Nucleotide Polymorphisms

SOD1 Superoxide Dismutase

SOD2 Manganese Superoxide Dismutase

ssODN single stranded oligonucleotide

TBS Tris Buffered Saline

TMRM Tetramethylrhodamine methyl ester

UPD7 Uniparental disomy 7

WES Whole Exome Sequencing

Abstract

Loss-of-function mutations in *SPART* gene cause Troyer syndrome, a recessive form of spastic paraplegia resulting in muscle weakness, short stature and cognitive defects. *SPART* encodes for Spartin, a protein linked to endosomal trafficking and mitochondrial membrane potential maintenance. Here, we identified with whole exome sequencing (WES) a novel frameshift mutation in the *SPART* gene in two brothers presenting an uncharacterized developmental delay and short stature. Functional characterization in a SH-SY5Y cell model shows that this mutation is associated with increased neurite outgrowth. These cells also show a marked decrease in mitochondrial Complex I activity, coupled to decreased ATP synthesis and defective mitochondrial membrane potential. The cells also presented an increase in reactive oxygen species, extracellular pyruvate and NADH levels, consistent with impaired Complex I activity. In concordance with a severe mitochondrial failure, Spartin loss also led to an altered intracellular Ca^{2+} homeostasis that was restored after transient expression of wild-type Spartin.

Our data provide for the first time a thorough assessment of Spartin loss effects, including impaired Complex I activity coupled to increased extracellular pyruvate. In summary, through a WES study we assign a diagnosis of Troyer syndrome to otherwise undiagnosed patients, and by functional characterization we show that the novel mutation in *SPART* leads to a profound bioenergetic imbalance.

Introduction

Neurodevelopmental disorders affect 2–5% of individuals and are genetically heterogeneous (1). They constitute a large proportion of the life-long global health burden in terms of medical care, hospitalizations, and mortality (2). An example of a rare developmental disorder is Troyer syndrome (OMIM #275900), which is an autosomal-recessive form of hereditary spastic paraplegia (HSP) characterized by lower extremity spasticity and weakness, short stature, cognitive defects, distal amyotrophy and degeneration of corticospinal tract axons (3, 4, 5, 6). In Troyer syndrome loss-of-function mutations occur in the *SPART* gene, which codes for Spartin, a multifunctional protein consisting of a N-terminal Microtubule Interacting and Trafficking (MIT) domain and a C-terminal senescence domain (7, 8) (Supplementary Fig. 1A). Spartin is expressed in a wide range of tissues at embryonic and adult stages. In the Eurexpress mouse database (http://www.eurexpress.org) expression of the homologous murine *Spg20* was identified in the nervous and olfactory systems of the developing mouse at embryonic day 14.5 (9). In the Human Protein Atlas *SPART* is ubiquitously expressed, with a high expression level in the central nervous system, gastrointestinal tract and reproductive system (https://www.proteinatlas.org/ENSG00000133104-SPG20). Spartin functions in a range of cellular processes including epidermal growth factor receptor trafficking, lipid droplets turnovers, bone morphogenetic protein (BMP) signalling and cytokinesis (8-14). Specifically, the impaired cytokinesis in *Spg20*-/- mice leads to a prominent number of binucleated chondrocytes in epiphyseal growth plates of bones, accounting for the short stature and skeletal defects observed in Troyer syndrome (15).

Interestingly, a few studies suggested that Spartin loss might impair mitochondrial function, documenting alterations in the mitochondrial network and decreases in the mitochondrial membrane potential (16-19).

In this study we used whole exome sequencing analysis, to identify a novel mutation in *SPART* gene in two brothers born from healthy consanguineous parents (first degree cousins). The brothers had been referred for pre- and post-natal growth retardation, syndromic short stature and developmental delay with severe speech impairment, and both carried a homozygous mutation, c.892dupA, which confers a premature stop codon. Although Troyer syndrome had not been considered in these two particular cases, a careful re-evaluation identified common features and we therefore investigated effects of this SPART loss-of-function mutation, which specific focus on mitochondria. We first evaluated the effects of Spartin loss using gene silencing in human neural stem cells (hNSCs), documenting altered neuronal growth and exhibited significantly longer neurites, compared to cells transfected with siRNA. We next generated a neuroblastoma-derived SH-SY5Y cell line carrying the mutation via CRISPR/Cas9-genome editing. Compared to control SH-SY5Y cells, the mutant cells exhibited increased neurite outgrowth and altered distribution and structure of the mitochondrial network. Importantly these cells also showed metabolic changes with severe decrease in Complex I activity, increased production of mitochondrial reactive oxygen species (ROS) and elevated extracellular pyruvate, which reflects defective mitochondrial oxidation of this molecule. Interestingly, in a recent study heterologous expression of human or *Drosophila* Spartin extended yeast lifespan, reduced age-associated ROS production and cell death (19). Spartin localized to the proximity of mitochondria, physically interacting with proteins related to mitochondrial and respiratory metabolism in yeast (19). Nevertheless, a thorough analysis of human *SPART* mutation effects in a human genome-edited neuronal cell model, including a quantitative mitochondrial respiration and OXPHOS activity assessment, has not been carried out yet. Our novel findings related to Spartin loss might provide clues to the neurological impairments in Troyer syndrome. Our data suggest that the mitochondrial impairment could affect neurons by inducing an energetic failure that could be coupled to excessive ROS production and extended axonal morphology.

In summary, through a WES study we were able to assign a diagnosis of Troyer syndrome to otherwise undiagnosed patients, and by functional characterization we elucidated that the novel mutation in *SPART* led to a profound bioenergetic imbalance.

Patients and methods

Subjects

Two brothers born from consanguineous healthy parents, first-degree cousins of Moroccan origin, were first evaluated at the Clinical Genetics Unit when they were 42-months and 12-months-old, respectively. Family history was unremarkable. They both presented with IUGR (intrauterine growth restriction), stature and weight below -2 SD (standard deviations), relative *macrocrania*, dysmorphic features (very long eyelashes, dolichocephaly, prominent maxilla, *pectus excavatum*) and mild psychomotor retardation, with severe language delay. They started walking independently at 18 months. Other shared anomalies included delayed bone age, *pes planus*, euphoric behavior, and joint hyperlaxity. The first evaluation did not disclose signs of neuromuscular involvement. Genetic analyses included: karyotype and analysis of subtelomeric regions, UPD7 and H19 methylation analysis, and mutation screening of *PNPLA6* (OMIM#603197), all of which were negative.

After a 5 years follow-up, the eldest brother (age 8 years and 9 months) gradually developed muscular hypotrophy in upper and lower limbs, increased muscle tone in the lower limbs (distal>proximal) and brisk deep tendon reflexes. Sporadic aggressive behavior and inappropriate crying was reported by parents. The younger sib (6 years and 3 months) developed muscular hypotrophy as well, mild hyper-reflexia and difficulty to walk on toes or heels. No cerebellar signs were reported, nor dysarthria/tongue dyspraxia but language impairment remained severe. Stature was constantly around the 3rd percentile in both sibs. The eldest brother showed a partial Growth Hormone (GH) deficiency, treated with a GH analogue.

High-throughput SNP genotyping and Whole Exome Sequencing (WES)

High-Throughput SNP genotyping

High-throughput SNP (Single Nucleotide Polymorphisms) genotyping was performed on Illumina Infinium HD Assay Gemini platform (Illumina, San Diego, CA, USA), according to manufacturer's protocol, starting from 400 ng of genomic DNA from peripheral blood. Genotypes were converted into PLINK format with custom scripts. PLINK v1.07 (http://ngu.mgh.harvard.edu/~purcell/plink/) was used to isolate individual Runs Of Homozygosity (ROH) that showed > 1 Mb overlap between the three affected siblings (20).

Whole Exome Sequencing (WES)

WES was performed on genomic DNA extracted from peripheral blood (QIAGEN, Hilden, Germany) from the two affected brothers. Genomic DNA libraries, starting from 100 ng genomic DNA, were prepared using the Illumina Pair-End Nextera Kit (Illumina) and library was enriched for exomic sequences using the Nextera coding exome kit. The captured regions were sequenced on the Illumina HiScanSQ platform for 200 cycles (100 cycles paired-ends, Illumina). The read files were aligned to hg19 version of the human genome sequencing, annotation and variant prioritization was performed according to our internal pipeline for exome annotation as previously reported (21). The identified variants were confirmed by Sanger sequencing.

Cell lines

SH-SY5Y cells (ATCC, Middlesex, UK) were cultured in Dulbecco's modified Eagle's medium (DMEM; Euroclone, Milan, Italy) supplemented with 10% (v/v) fetal bovine serum, 100 U/mL penicillin and 100 µg/mL streptomycin (Sigma-Aldrich, St. Louis, MO, USA).

Human neural stem cells (hNSC), derived from the NIH approved H9 (WA09; WiCell Research Institute, Madison, WI, USA) human embryonic stem cells (hESCs), were grown in 6-well plates coated with CTS™ CELLstart™ Substrate (Gibco, Thermo Fisher Scientific, Waltham, MA, USA) and maintained in KnockOut D-MEM/F-12 with 2mM of GlutaMAX-I supplement, 20 ng/ml of bFGF, 20 ng/ml of EFG and 2% of StemPro® Neural Supplement (Thermo Fisher Scientific). All cells were grown in a humidified incubator with 95% air and 5% CO_2 at 37°C.

Silencing SPART in Neural Stem Cells (hNSC)

To transiently knock-down *SPART*, hNSC were transfected every 36 hours with a combination of 3 siRNAs (Thermo Fisher Scientific; see Supplementary Table 1 for the sequences), using Lipofectamine3000 (Thermo Fisher Scientific) according to the manufacturer's instruction. At day 0, 4 and 8 cells were collected and processed for western blot and imaging analysis.

Generation of SPART c.892dupA knock-in SH-SY5Y cell line

The *SPART* mutation was generated in SH-SY5Y genome using guide RNAs (gRNAs) designed with the CRISPR Design Tool (mit.edu.crispr) (22). Annealed oligos containing the target sequence for Cas9 were cloned into pSpgRNA that expresses gRNA driven by a U6 promoter (*S. pyogenes* Cas9 guide RNA #47108; Addgene, Cambridge, MA, USA, 23) and sequenced. Sequences of gRNAs and single stranded-oligonucleotide (ssODN) carrying the variant c.892dupA are reported in Supplementary Table 1. Cells were plated at 80% confluence and transfected with 4.7 µg of pSpCas9n(BB)-2A-GFP (PX458, #48140; Addgene; 24), 0.8 µg of each gRNA expression plasmid and 10 µM of ssODN with Lipofectamine®3000 (Thermo Fisher Scientific) according to the manufacturer's instruction. After 28 hours, cells were sorted with an automated Fluorescence-Activated Cell Sorting (FACS) system (Influx, Becton Dickinson, Franklin Lakes, NJ, USA) and single cells were plated in 96-well plates coated with Poly-D-Lysine (Sigma-Aldrich). Clones were amplified and screened by PCR and direct sequencing of the target region. A clone carrying the specific change and with no off-target mutations was selected for the analysis (hence defined *SPART*^{892dupA}). The SH-SY5Y clone that underwent the same CRISPR/Cas9 genome editing approach but did not carry any change was used as control cell line (hence defined *SPART*^{wt} throughout the text).

Western blotting

Cells were lysed in ice-cold RIPA buffer: 50 mM HEPES (EuroClone), 1 mM EDTA (Sigma-Aldrich), 10% glycerol (Thermo Fisher Scientific), 1% Triton X-100 (Sigma-Aldrich), 150 mM NaCl in the presence of proteases and phosphatases inhibitors (Sigma-Aldrich). Total protein was measured using the Lowry protein assay kit (Bio-Rad DC Protein Assay; Bio-Rad, Hercules, CA, USA) according to the manufacturer's instruction. Protein samples (70 μg) were subsequently separated on 10% sodium dodecyl sulfate polyacrylamide electrophoresis (SDS-PAGE) gels or on 4-20% pre-cast SDS-PAGE gels (Bio-Rad). Gels were then electro-transferred onto nitrocellulose membranes (Trans-Blot Turbo Transfer System, Bio-Rad). Membranes were blocked in Tris Buffered Saline (TBS) with 1% Casein (Bio-Rad) for 1 hour at room temperature and incubated with primary antibodies at 4°C for 16 hours. Membranes were washed three times in Tris-buffered saline containing 0.1% Tween and incubated with peroxidase-conjugated secondary antibodies for 45 minutes at room temperature. Bands were visualized using WESTAR Supernova (Cyanagen, Bologna, Italy) and detected with the ChemiDoc™ XRS+ system (Bio-Rad). Densitometric analysis was performed with ImageLab software (Bio-Rad). Primary antibodies used were: GAPDH (mouse, 1:10,000; Abcam, Cambridge, UK), γ-tubulin (mouse, 1:10,000; Sigma-Aldrich), T-STAT3 (mouse, 1:500; OriGene, Rockville, MD, USA), P-STAT3 (rabbit, 1:500; Cell Signaling, Leiden, Netherlands), Spartin (rabbit, 1:1,000; 13791-1-AP, N-terminal; ProteinTech, Rosemont, IL, USA) and GRP75 (goat, 1:500; Santa Cruz, CA, USA). Peroxidase-conjugated secondary antibodies used were anti-mouse IgG (1:5,000), anti-rabbit IgG (1:5,000; Sigma-Aldrich), anti-goat IgG (1:5,000; Dako, Glostrup, Denmark).

Immunofluorescence microscopy

Cells were plated in ibiTreat μ-Slide 8 Well (Ibidi, Martinsried, Germany). When 80% confluent, they were fixed in 4% paraformaldehyde in PBS for 10 minutes at 4°C. Samples were blocked and permeabilized in 10% newborn calf serum (Sigma-Aldrich), 0.3% Triton X-100 (Sigma-Aldrich) in

PBS for 1 hour at room temperature. Samples were incubated 16 hours at 4°C in primary antibody diluted in 5% newborn calf serum, 0.15% Triton X-100 in PBS. After three 30-minutes washes in PBS, sample were incubated 16 hours at 4°C in secondary antibodies diluted in 5% newborn calf serum, 0.15% Triton X-100 in PBS. After three 30-minutes washes in PBS, samples were mounted in Fluoroshield containing DAPI (4′,6-diamidino-2-phenylindole; Sigma-Aldrich). Microscopies used for imaging were Leica DM5500B equipped with a Leica DCF3000 G camera (Leica Mikrosysteme Vertrieb GmbH, Wetzlar, Germany) and Axiovert 200 inverted microscope (Carl Zeiss, Oberkochen, Germany). Primary antibodies were as follows: α-III tubulin (mouse, 1:500; Abcam), Spartin (rabbit, 1:1,000; ProteinTech), Nestin (mouse, 1:300; Abcam) and PGP9.5 (rabbit, 1:300; Thermo Fisher Scientific), and secondary antibodies: Alexa Fluor 488 goat anti-rabbit IgG, Alexa Fluor 488 donkey anti-mouse, Alexa Fluor 555 goat anti-rabbit and Alexa Fluor 555 donkey anti-mouse (all diluted 1:800; Abcam). Quantitative evaluation of α- tubulin, Spartin and Nestin fluorescence intensity have been performed using ImageJ.

RNA isolation and quantitative PCR (qPCR) in cell lines

Total RNA was isolated from SH-SY5Y cultures using the RNeasy Mini Kit (QIAGEN). cDNA from 1 µg of $SPART^{wt}$ and $SPART^{892dupA}$ RNA was synthesized using the SuperScript™ VILO™ cDNA Synthesis Kit (Thermo Fisher Scientific). Quantitative PCR was performed using SYBR® Green master mix (Bio-Rad). All samples were run in triplicate on the ABI7500 Fast PCR machine (Thermo Fisher Scientific). Melting curve analysis for each primer pair was carried out to ensure specific amplification. Relative mRNA expression levels of *CAT, SOD1, SOD2* were normalized to the house-keeping gene β-actin using the ΔΔCt method. Primers are reported in Supplementary Table 1.

Quantification of neurite outgrowth and elongation

Cells were seeded on Poly-L-Lysine (Sigma-Aldrich) coated glasses and immunofluorescence for the neuronal marker PGP9.5 was performed as described above. Mean neurite number and length was measured using the NeuronGrowth plugin (ImageJ, National Institute of Health, Bethesda) by tracing the individual neurites of cells according to Fanti *et al.* (25). For each experiment twenty cells were examined.

Spheroid formation assay

We generated matrix-free SH-SY5Y spheroid cultures by seeding $2x10^4$ *SPART*^{wt} and *SPART*^{892dupA} SH-SY5Y cells in ultra-low attachment µ-slide 8-wells (Ibidi). Cells were grown to allow the spontaneous formation of spheroids. After 4 days, spheroids were examined and photographed using an Axiovert 200 inverted microscope (Carl Zeiss), then RNA was extracted. Spheroids morphology was measured using ImageJ software.

ROS quantification

Intracellular ROS measurement using DCFDA

Control and *SPART*^{892dupA} SH-SY5Y cell lines were seeded at 5×10^3 cells/well and incubated overnight. Cells were treated with 10 µM DCFDA (2',7'–dichlorofluorescin diacetate, Sigma-Aldrich) dissolved in medium for 1 hour. Cells were washed with PBS and the fluorescence emission from each well was measured (λ Excitation = 485 nm; λ Emission = 535 nm) using a multi-plate reader (Enspire, Perkin Elmer, Waltham, MA, USA) and normalized for protein content using a Lowry assay. Data are reported as the mean ± standard deviation of at least three independent experiments.

Mitochondrial ROS measurement using MitoSOX

Mitochondrial superoxide production was measured using MitoSOX™ Red (Molecular Probes, Thermo Fisher Scientific) following manufacturer instructions with minor modifications. Briefly, cells were seeded in 96-well plates (OptiPlate black, Perkin Elmer) at 5×10^3 cells/well and incubated for 16 hours to allow adhesion. Cells were then treated with 5 µM MitoSOX Red dissolved in medium for 30 minutes. Cells were washed twice times with warm PBS and the fluorescence emission from each well was measured (λ Excitation = 510 nm; λ Emission = 580 nm) using a multi-plate reader (Enspire, Perkin Elmer) and normalized for protein content using a Lowry assay. Data are reported as the mean ± standard deviation of at least six independent experiments.

Mitochondrial network and morphology assessment via live cell imaging

To visualize the mitochondrial network in live cells, $3×10^4$ cells were plated in ibiTreat µ-Slide 15 Well (Ibidi, Germany) in 50 µl of complete medium and incubated at 37°C in a humidified atmosphere of 95% air/5% CO_2. After 24 hours, cells were transfected with a plasmid carrying the GFP protein targeted to mitochondria, following the manufacturer's instructions (CellLight™ Mitochondria-GFP, BacMam 2.0, Thermo Fisher Scientific). Mitochondrial network morphology was assessed by live cell imaging, using a Nikon C1si confocal microscope (Nikon, Tokio, Japan) following the procedure of Dagda *et al.* (26) with minor modification using ImageJ software. Briefly, the green channel was subjected to both a background subtraction with a radius of 10 pixels and a median filter to reduce noise. An automatic threshold value was then applied to delineate the particles. The mean area/perimeter ratio was employed as an index of mitochondrial interconnectivity according to the previously published method reported in Dagda *et al*. (26).

Mitochondrial three-dimensional (3D) network analysis

In order to visualize the 3D structure of the mitochondrial network, cells were plated in ibiTreat µ-Slide 8 Well (Ibidi, Martinsried, Germany). After 24 hours, cells were transfected with a plasmid carrying the GFP protein targeted to mitochondria as described above. The mitochondrial 3D network analysis was performed according to Giuliani *et al.* (27). Briefly, cell preparations were scanned with a Nikon Ti-E fluorescence microscope coupled to an A1R confocal system and the

NIS-Elements AR 3.2 software. An air-cooled argon-ion laser system with 488 wavelength output was used. Images were acquired with oil immersion (60x) with an optical resolution of 0.18 micron, 3 x scanner zoom, and 1024 x 1024 pixel resolution. All the stacks were collected with optical section separation (interval) values suggested by the NIS-Elements AR 3.2 software (0.5μm step). Five randomly selected fields per sample were acquired. 3D images were analyzed by the IMARIS software (Bitplane, Concord, MA, USA). The software analyzes the volumes of all detected isosurfaces and calculates the average value, corresponding to the average volume of interconnected mitochondria per cell. This analysis allows to measure the average volume of single interconnected mitochondrial isosurfaces, directly linked to mitochondrial fragmentation.

Mitochondrial oxygen consumption

To measure mitochondrial oxygen consumption in $SPART^{wt}$ and $SPART^{892dupA}$ cells, $1.5x10^6$ cells for each cell line were harvested at 70-80% confluence, washed in PBS, re-suspended in complete medium and assayed for oxygen consumption at 37°C using a thermostatically regulated oxygraph chamber (Instech Mod.203, Plymouth Meeting, PA, USA) in 1.5 ml of culture medium. Basal respiration was compared with the one obtained after injection of oligomycin (1 μM). FCCP (1–6 μM). Antimycin A (5 μM) was added at the end of experiments to completely block mitochondrial respiration. The respiratory rates were expressed in μmol O_2/min/mg of protein referring to 250 nmol O_2/ml of buffer as 100 % at 30°C (28). Data were normalized to protein content determined using the Lowry assay.

ATP and ADP determination

Nucleotides were extracted and detected following Jones DP, 1981 (29), using a Kinetex C18 column (250 × 4.6 mm, 100 Å, 5 μm; Phenomenex, CA, USA). Absorbance (260 nm) was monitored with a photodiode array detector (Agilent 1100 series system). Nucleotide peaks were identified by comparison and coelution with standards, and quantification by peak area measurement compared with standard curves. The ATP level was also measured in presence or absence of rotenone (a specific Complex I inhibitor, Sigma-Aldrich). $4x10^5$ *SPART*^{wt} and *SPART*^{892dupA} cells were seeded and treated with 200 nM of rotenone for 72 hours, then ATP level was measured as describes above.

Respiratory chain complex activities

Cell lysates were resuspended in a 20 mM hypotonic potassium phosphate buffer (pH 7.5) followed by spectrophotometric analysis of mitochondrial complexes activity at 37°C using a Jasco-V550 spectrophotometer (Jasco, Easton, MD, USA) equipped with a stirring device. Complex I activity was measured in 50 mM phosphate buffer at 340nm (ε=6.22 mM^{-1} cm^{-1}) after the addition of 150 µg of cell lysate, 1 mM KCN, 10 µM antimycin a, 2.5 mg fatty acid-free BSA, 100 µM NADH, 60 µM decylbenzoquinone (DB, Sigma-Aldrich). Complex I (NADH dehydrogenase) specific activity was obtained by inhibiting complex I with 10 µM rotenone. The succinate-cytochrome c reductase activity (II+III activity) was measured in 50 mM phosphate buffer at 550 nm (ε=18.5 mM^{-1} cm^{-1}) after the addition of 100 µg of cell lysate, 1 mM KCN, 20 mM succinate and 50 µM oxidized cytochrome c. The specific complex II+III activity was obtained by inhibiting complex II with 500 µM TTFA. The NADH-cytochrome c reductase activity (I+III activity) was measured in 50 mM phosphate buffer at 550 nm (ε=18.5 mM^{-1} cm^{-1}) after the addition of 100 µg of cell lysate, 1 mg/ml of fatty acid-free BSA, 1 mM KCN, 50 µM cytochrome c and 200 µM NADH. The specific complex I+III activity was obtained by inhibiting complex I with 10 µM rotenone. Citrate synthase activity was measured in 100 mM TRIS buffer with 0,1% Triton X-100 at 412 nm (ε=13,600 $M^{-1}cm^{-1}$) after the addition of 30 µg of cell lysate, 0.1 mM acetyl-CoA, 0.5 mM oxaloacetate, and 0.1 mM 5,5′-dithiobis-2-nitrobenzoic acid (DTNB; Sigma-Aldrich).

Mitochondrial transmembrane potential (m$\Delta\psi$)

Mitochondrial transmembrane potential and mass were measured following Kirk *et al*. (30) with minor modifications. Briefly, cells were seeded at the density of 10^4 cells/well in 96-well culture plates (OptiPlate Black, Perkin Elmer). After 24 hours, cells were loaded with 50 nM tetramethylrhodamine methyl ester (TMRM, 544 Excitation; 590 Emission, Thermo Fisher Scientific) and 25 nM MitoTracker Green (MTG, 490ex; 516em, Thermo Fisher Scientific) for 30 minutes and washed twice with PBS. The fluorescence emission from each well was measured with a multi-plate reader (Enspire, Perkin Elmer). TMRM fluorescence emission intensity was normalized by comparing to MitoTracker Green fluorescence.

NADH quantification

NADH autofluorescence measurements were performed as described by Frezza *et al.*, 2011 (31) with minor modifications. Briefly, cells were seeded at a density of $3x10^3$ cells/ well in 15-well µ-Slides (Ibidi) following manufacturer's instructions and incubated for 16 hours to allow adhesion. Images were collected using a Nikon C1si confocal microscope equipped with UV laser. NADH quantification was performed using ImageJ software after background subtraction.

Lactate and pyruvate quantification

Extracellular lactate was determined by HPLC (High Performance Liquid Chromatography). Briefly, cells were seeded in 6-well dishes and after 72 hours the culture medium was collected for HPLC analysis. Prior to injection, the culture medium was diluted 1:10 in mobile phase and centrifuged at 14,000 g for 5 minutes at 4°C. The supernatant was then injected manually into the HPLC system. Metabolites were separated on a C18 column (Agilent ZORBAX SB-Phenyl, 5 µm, 250×4.6 mm, Santa Clara, CA, USA), using a mobile phase consisting of 50 mM KH_2PO_4, pH 2.9, at a flow rate of 0.8 ml/min. Lactate and pyruvate were detected using an Agilent UV detector set to 210 nm and quantified using Agilent ChemStation software. The retention time was determined by injecting standard solution. All injections were performed in triplicate. The peak area was normalized forprotein content as measured using a Bradford assay.

Measurement of intracellular Ca^{2+}

Intracellular calcium level was assessed in live cells using Fura-2 AM probe (Thermo Fisher Scientific) following manufacturer's instruction. The emission of the calcium-free probe was measured using a Nikon C1si confocal microscope (Nikon, Tokio, Japan) at λ = 380 nm Excitation and λ = 515 nm Emission. The quantification of fluorescence intensity was carried out using the ImageJ software, with an automated acquisition of Fura-2 AM probe fluorescence (at least 50 cells per condition were acquired).

Rescue of the phenotype with Spartin wild type

Human *SPART* coding sequence was PCR-amplified from SH-SY5Y-derived cDNA using the KAPA HiFi HotStart Taq Polymerase (Kapa Biosystems, Roche Diagnostic, Mannheim, Germany) according to the manufacturer's instructions. Primers are reported in Supplementary Table 1. The amplified fragment was digested with *XhoI* and *HindIII* (New England Biolabs, Hitchin, UK), cloned in pcDNA3.1 vector and sequenced to verify the correct insertion. For rescue experiments, $4x10^5$ $SPART^{wt}$ and $SPART^{892dupA}$ cells were plated. The plasmids expressing wild-type *SPART* (3 μg/experiment) was transfected into $SPART^{892dupA}$ cells using Lipofectamine 3000 (Life Technologies) following the manufacturer's instructions. In parallel, the pcDNA3.1 empty vector (3 μg/experiment) was transfected into $SPART^{wt}$ and $SPART^{892dupA}$ cells. Forty-eight hours after transfection, cells were pelleted and washed twice with PBS. Western blot analysis was used verify Spartin overexpression, determination of ATP and ADP synthesis and assessment of intracellular Ca^{2+} were performed as previously described.

Gene expression of spg20b in zebrafish developmental stages and zebrafish adult tissues

Total RNA from developmental stages between 16–32 cells, up to 120 hours post-fertilization (hpf) was extracted using the RNeasy Mini kit according to the manufacturer's instructions (QIAGEN) using at least 50 embryos at each stage. Heart, liver and brain were dissected from 5 adult fish, flash-frozen on dry ice and stored at -80°C until the RNA was extracted. Animals were handled following the guidelines from European Directive 2010/63/EU and euthanised with Schedule 1 procedures of the Home Office Animals (Scientific Procedures) Act 1986. RNA was synthesized using the SuperScript™ VILO™ cDNA Synthesis Kit (Thermo Fisher Scientific) following the manufacturer's protocol. Gene expression level of *spg20b* was assessed using quantitative PCR (qPCR) conducted with the SYBR Green master mix (Bio-Rad). All samples were run in triplicate on the ABI7500 Fast PCR machine (Thermo Fisher Scientific). Relative mRNA expression level of *spg20b* was normalized to the eukaryotic translation *eef1a1l2* as endogenous control gene. Primers are reported in Supplementary Table 1. All zebrafish studies were approved by the Animal Welfare and Ethics Committee at the University of St. Andrews.

Image analysis

Images were analyzed using ImageJ (public software distributed by the National Institutes of Health), Chemidoc (Bio-Rad) and IMARIS (Bitplane).

Statistical analysis

Statistical analysis was conducted with Prism 7 (GraphPad, San Diego, CA, USA). All experiments were carried out at least in triplicates. Results are expressed as the mean ± SEM. Unpaired Student's t-test with Welch's correction, Fisher's exact test or ANOVA test with Tukey-multiple comparison test were used to determine the differences between groups, when appropriate. A p-value <0.05 (two-tailed) was considered statistically significant.

Results

Whole exome sequencing identified a novel loss-of-function mutation in *SPART* gene

We performed a combined analysis of high-density SNPs genotyping and WES in the two affected brothers (Fig. 1A: II-1, II-2) born to consanguineous partners. The two siblings presented with a history of intrauterine growth restriction, stature and weight below -2 SD, relative *macrocrania*, dysmorphic features (very long eyelashes, dolichocephaly, prominent maxilla, *pectus excavatum*, Fig. 1B) and psychomotor retardation, with severe language delay (for an exhaustive description of cases see the Materials and Methods section). In consideration of the degree of inbreeding, a search for runs of homozygosity (ROH) using SNP data from Illumina 350K array identified a region of homozygosity on chromosome 13 (5 Mb). WES analysis identified a novel insertion on chr13:g3690561insT (hg19), leading to a c.892dupA (NM_001142294) in the *SPART* gene (OMIM *607111). The mutation was homozygous in the two affected sibs and caused a frameshift with the insertion of a premature stop codon (p.Thr298Asnfs*17) in the protein Spartin. The variant was carried by the parents (Fig. 1A, I-1 and I-2) and was not present in the Exome Aggregation database (ExAc) and Genome Aggregation database (gnomAD) (as accessed on 20/11/2018), nor in an in-house whole exome database consisting of 650 exomes.

Generation of biological models

To understand the effect of *SPART* ablation we generated two biological models. First, we transiently silenced *SPART* with siRNA in human Neural Stem cells (hNSCs), using siRNA specific to *SPART* transcripts *vs* cell treated with scramble siRNA. Silencing efficiency was evaluated using western blot analysis (Supplementary Fig. 1B). Second, we generated a stable SH-SY5Y cell line with a knock-in of the c.892dupA mutation using the CRISPR/Cas9 technology.Cells were transfected with paired gRNAs and Cas9-nickase plasmids and the oligo DNA carrying the c.892dupA variant to insert the specific modification into the SH-SY5Y genome (Fig. 1C). The variant is predicted to generate a shorter protein of 33KDa, however western blot analysis showed that Spartin in *SPART*^{892dupA} cells was completely absent (Fig. 1D).

Spartin depletion affects neuronal morphology leading to neuronal differentiation

To understand the effect of *SPART* loss on neuronal morphology, we transiently silenced the gene in hNSCs up to 8 days of treatment, using siRNA specific to *SPART* transcripts *vs* scrambled siRNA (Fig 2A, B). In *SPART*-silenced hNSCs, we observed an increased neurite outgrowth, visualized via nestin staining (Fig. 2A, panel f and Fig. 2B, panel a) compared to scramble-treated hNSCs (Fig. 2A, panel e and Fig. 2B, panel b). After 8 days of *SPART* silencing, we found no significant differences in α-tubulin and nestin expression between scramble-transfected and *SPART*-silenced hNSCs (Student's t-test with Welch's correction, p=0.5394 and p=0.9883 respectively, Supplementary Fig. 1C-D). At day 8, in agreement with western blot data (Supplementary Fig. 1B), Spartin staining was not detectable in *SPART*-silenced hNSCs, as compared with those treated with scrambled siRNA (Student's t-test with Welch's correction, p<0.0001, Supplementary Fig. 1E).

In the stable knock-in cell line carrying the c.892dupA mutation, immunostaining for PGP9.5 (a specific neuronal marker localized to cell bodies and neurites) revealed an altered neuronal morphology compared to control *SPART*^{wt} cells (Fig. 2C). *SPART*^{892dupA} cells showed extensive and branched neurite-like formations (Fig. 2C, panels g, h) compared to *SPART*^{wt} (Fig. 2C, panels c, d). Neuritogenesis was measured using a quantitative evaluation of the length and number of neurites using the NeuronGrowth software. *SPART*^{892dupA} cells showed significantly longer neuronal processes, compared to *SPART*^{wt} cells (Student's t-test with Welch's correction, p=0.0001; Supplementary Fig. 1F) and an increase in average number of neurites per cell extending from the cell body (Student's t-test with Welch's correction, p=0.0337; Supplementary Fig. 1G).

Moreover, Spartin-depleted cell models (both hNSC and SH-SY5Y) presented an extensive cell loss compared to controls (Fig. 2D, 2E).

Spartin loss alters cell morphology in 3D cultures

Since the data on $SPART^{892dupA}$ cell extended neurites suggested an altered neuronal differentiation, we evaluated cell morphology in a matrix-free environment. When cells were shifted from a 2D to a 3D micro-environment (spheroids), $SPART^{wt}$ and $SPART^{892dupA}$ cultures showed a different morphology. Twenty-four hours after seeding both cell lines started to aggregate, and they grew into spheroids-like structures at 72 hours (Fig. 3A). $SPART^{wt}$ cells formed condensed and disorganized aggregates (Fig. 3A, panels b, c), whereas $SPART^{892dupA}$ cells formed rounder and more compact aggregated more similar to spheroids (Fig. 3A, panels e, f). These differences, already detectable at 24 hours, were confirmed by the quantitative measurement of spheroid circularity at 24 and 72 hours, using ImageJ software. We found increased circularity for $SPART^{892dupA}$-derived spheroids compared to $SPART^{wt}$, both at 24 and 72 hours (Student's t-test with Welch's correction, $p<0.0001$ and $p=0.0001$ respectively, Fig. 3B). According to the classification of Kenny *et al*. (32), $SPART^{892dupA}$-derived spheroids could be classified as "round group", characteristic of non-malignant and more differentiated cells, since there was a prevalence of rounded spheroids. $SPART^{wt}$-derived spheroids could be classified in the "grape-like" group, characterized by cancer stem cell-like properties, with high frequency of disorganized formations (88 round spheroids and 9 grape-like spheroids for $SPART^{892dupA}$ cells vs 11 round spheroids and 55 grape-like spheroids for $SPART^{wt}$ cells; Fisher's exact test, $p<0.0001$, Fig. 3C, D).

Spartin loss alters the mitochondrial network

Previous studies showed that Spartin co-localized with mitochondria and contributed to mitochondrial stability (16, 18, 33). Therefore, we evaluated the effects of the c.892dupA mutation on different mitochondrial characteristics. Assessment of mitochondrial network was performed using live-cell microscopy in mitoGFP-transfected cells (Fig. 4A). The total mitochondrial mass per cell was similar between $SPART^{wt}$ and $SPART^{892dupA}$ cells (Supplementary Fig. 1H) but decrease in the total number of mitochondria was observed in neurite-like extensions in mutants compared to controls (Fig. 4A, arrows). *SPART*^{892dupA} cells displayed a fragmented and disorganized mitochondrial network morphology (Fig. 4A, right panel) compared to control cells (Fig. 4A, left panel). In particular, we found a decrease of the mean perimeters (Student's t-test with Welch's correction, $p=0.0242$), mean areas ($p=0.0117$), and an increase of roundness value ($p<0.0001$) of mitochondria in mutant cells compared to controls (Fig. 4B; mitochondria in n=35 cells for each cell lines were measured). Moreover, mitochondria in *SPART*^{892dupA} cells exhibited a decreased interconnectivity, indicated by a decreased area-to-perimeter ratio, compared to the *SPART*^{wt} control cells (Student's t-test with Welch's correction, $p<0.0001$; Fig. 4C).

In order to further analyze the altered connectivity of the mitochondrial network due to Spartin loss, we performed a three-dimensional acquisition of mitochondrial-GFP transfected cells with confocal microscopy. Z-stacks were analyzed using IMARIS software, in order to quantify the mean volume of the isosurfaces reconstructed from GFP fluorescence and representing the mitochondrial network. The 3D view of the mitochondrial network emphasized the fragmented organization in cells lacking Spartin (Fig. 4D). The analysis showed a strong reduction in the mean volume per cell of the elaborated network, in *SPART*^{892dupA} compared to *SPART*^{wt} (Student's t-test with Welch's correction, $p=0.0237$; Fig. 4E). These data support the hypothesis that Spartin loss might cause mitochondrial network fragmentation.

Spartin loss determines a specific OXPHOS Complex I impairment

Mitochondrial morphology reflects its functionality (34), therefore we measured the oxygen consumption rates in *SPART*^{wt} and *SPART*^{892dupA} intact cells, in absence and in presence of the specific ATPase inhibitor oligomycin A and of carbonyl cyanide-4-(trifluoromethoxy) phenylhydrazone (FCCP) as uncoupling agent. No difference in endogenous respiration (basal) was observed, but the uncoupled oxygen consumption (FCCP) was significantly decreased in *SPART*^{892dupA} mutant cells (n=3 independent experiments, one-way ANOVA with Tukey's multiple comparisons test, p=0.0173; Fig. 5A). We found that cells lacking Spartin exhibited a significantly lower ATP/ADP ratio in comparison to controls, due to the concomitant decrease of ATP and increase of ADP levels (n=3 independent experiments, Student's t-test with Welch's correction, p=0.0065; Fig. 5B).We investigated the OXPHOS enzyme activities by measuring: NADH-cytochrome c oxidoreductase activity (Complex I+III); succinate dehydrogenase-cytochrome c oxidoreductase activity (Complex II+III) and NADH-DB oxidoreductase activity (Complex I). *SPART*^{892dupA} mutant cells showed a 50% decrease of Complex I+III and Complex I activities (n=3 independent experiments, Student's t-test with Welch's correction, p<0.0001 and p=0.0268 respectively; Fig. 5C, D), whereas no difference compared to controls was found for Complex II+III activity (p=0.6485; Fig. 5E). These data show that cells lacking Spartin presented a Complex I impairment. To further investigate the effect of Spartin on Complex I activity, we measured the ATP level in *SPART*^{wt} and *SPART*^{892dupA} grown for 72 hours in the presence and absence of 200 nM of the specific Complex I inhibitor rotenone. *SPART*^{wt} cells were significantly impaired in ATP synthesis in presence of rotenone (n=4 independent experiments, one-way ANOVA with Tukey's multiple comparisons test, p=0.0077; Fig. 5F), whereas *SPART*^{892dupA} were less sensitive to rotenone, since their Complex I activity was already severely impaired by the mutation in *SPART* (p=0.5496, Fig. 5F).

Consistently with an impaired OXPHOS Complex I activity, we observed a significant reduction (20%) in mitochondrial membrane potential in *SPART*^{892dupA} cells, compared to control cells (n=12 independent experiments, Student's t-test with Welch's correction, p<0.0001; Fig. 5G).

Altered pyruvate metabolism in *SPART*^{892dupA} mutant cells

Since OXPHOS respiration was impaired, we investigated a possible metabolic switch to glycolysis. We measured intracellular NADH levels and extracellular lactate. In *SPART*^{892dupA} mutated cells, the intracellular NADH level was increased in comparison to control cells (13 fields for each cell type, Student's t-test with Welch's correction, p=0.0026, Fig. 6A). HPLC analysis of extracellular culture medium did not detect any change in extracellular lactate levels (Fig. 6B). Nevertheless, in the extracellular culture medium of *SPART*^{892dupA} cells, we identified a 2.5 folds increase in pyruvate levels in comparison to controls (n=3 independent experiments, Student's t-test with Welch's correction, *SPART*^{892dupA} = 231.4±27.65 vs *SPART*^{wt} = 77.56±7.639; p=0.0241, Fig. 6C-D).

STAT3 activation in *SPART*^{892dupA} mutant cells

Decreased oxidative phosphorylation has been correlated to STAT3 activation, and constitutive activation of STAT3 in several cell models indicated a major role for this transcription factor in promoting increased glycolysis (35). Thus, we investigated the phosphorylation/activation status of STAT3 in mutant and control cell lines using western blot analysis of phosphorylated (p-STAT3) and total (T-STAT3) STAT3 protein. In *SPART*^{892dupA} cells STAT3 was phosphorylated, whereas no activation was observed in *SPART*^{wt} cells. Comparable levels of total STAT3 were present in both cell types (Fig. 6E).

Spartin loss increased mitochondrial Reactive Oxygen Species (ROS) and altered intracellular Ca^{2+} homeostasis

Increases in cellular superoxide production are implicated in a variety of pathologies, including neurodegeneration (36). Mitochondrial superoxide is generated as a by-product of oxidative phosphorylation and in healthy cells occurs at a controlled rate. Given the specific NADH-dehydrogenase activity (Complex I) impairment detected in mutant cells, we investigated whether ROS production was altered by Spartin loss. Intracellular ROS levels, measured with the fluorescent probe 2',7'–dichlorofluorescin diacetate (DCFDA), were significantly increased in *SPART*^{892dupA} cells (n=3 independent experiments, Student's t-test with Welch's correction, p<0.0001; Fig. 7A). Moreover, by staining live cells with MitoSOX™ Red, a highly selective probe for mitochondria-specific superoxide, we found a significant increase in superoxide production in $SPART^{892dupA}$ cells compared to the control (n=3 independent experiments, Student's t-test with Welch's correction, p<0.0001; Fig. 7B).To further investigate the oxidative stress status of mutated cells, we tested the expression of the major ROS-detoxifying enzymes. RT-qPCR revealed a significant reduction in expression of *CAT* (Catalase), *SOD1* (Superoxide Dismutase) and *SOD2* (mitochondrial Manganese Superoxide Dismutase) in cells lacking Spartin, compared to controls (n=3 independent experiments, Student's t-test with Welch's correction, p=0.0027 for *CAT*; p=0.0280 for *SOD1;* p=0.0172 for *SOD2*; Fig. 7C-E, respectively).

Glucose-Regulated Protein 75 (GRP75) has a major role in neuronal cells for mitochondrial function regulation and protection from stress-induced ROS and physically interacts with Spartin (36, 37). Therefore, we evaluated its protein levels, and found a higher expression of GRP75 in $SPART^{892dupA}$ compared to $SPART^{wt}$ cells (n=3 independent experiments, Student's t-test with Welch's correction, p=0.0327; Fig.7F).

GRP75 also coordinates the exchange and transfer of Ca^{2+}, thereby affecting mitochondrial function and intracellular Ca^{2+} homeostasis (37). Accordingly, we assessed intracellular free Ca^{2+} in $SPART^{wt}$ and $SPART^{892dupA}$ cells by quantifying Ca^{2+} probe Fura-2 AM-relative fluorescence. We found a significant increase of intracellular Ca^{2+} in $SPART^{892dupA}$ cells, compared to $SPART^{wt}$ cells (n=3 independent experiments, Student's t-test with Welch's correction, p<0.0001; Fig. 7G). These results are consistent with previous data showing that the decreased expression of Spartin via transient silencing led to a dysregulation of intracellular Ca^{2+} levels (18).

In order to provide additional evidence that these observed defects were specifically due to Spartin absence, we re-expressed Spartin in $\mathrm{SPART}^{892dupA}$ cells. Spartin re-expression in $SPART^{892dupA}$ cells rescued altered intracellular Ca^{2+}, restoring Ca^{2+} levels as in control cells (n=3 independent experiments, one-way ANOVA Tukey's multiple comparisons test, $SPART^{wt}$ *vs.* $SPART^{892dupA}$ p<0.0001; $SPART^{wt}$ *vs.* $SPART^{892dupA+\ SPART}$ p=0.5690; $SPART^{892dupA}$ *vs.* $SPART^{892dupA+\ SPART}$ p<0.0001; Fig. 7H).

642

Discussion

Next generation sequencing (NGS) technologies are powerful tools for the identification of rare mutations that cause neurodevelopmental disorders (38-44). The identification of a causative mutation can support diagnosis, prognosis, and available treatment (45). Using WES technology, we identified a novel homozygous insertion (c.892dupA) in the *SPART* gene in two male sibs with syndromic short stature, developmental delay and severe speech impairment, with consanguineous healthy parents. This novel *SPART* mutation generated a frameshift and a premature stop codon in the Spartin protein. Loss-of-function mutations in *SPART* cause Troyer syndrome (OMIM 275900), a very rare recessive form of HSP (3-6). Although Troyer syndrome was not firstly diagnosed, the WES data prompted a thorough clinical reassessment, that identified muscular hypotrophy in upper and lower limbs, increased muscle tone in lower limbs (distal>proximal) and brisk deep tendon reflexes, all symptoms characteristic of this specific HSP form due to mutations in the *SPART* gene (46).

Nonetheless, so far very few *SPART* loss-of-function mutations have been reported (3, 4, 6, 47-51, Supplementary Table 2). Animal (null mice) and cellular models (Spartin silencing/overexpression) showed a role for Spartin in different processes, including neuronal survival/sprouting, cell division and mitochondrial stability (7, 8, 10, 12, 13, 19).

Based on this evidence, we focused our functional studies to investigate the effect of *SPART* c.892dupA mutation on mitochondrial network integrity and mitochondrial functionality. We used two different cell models: hNSCs (silenced for *SPART*) and SH-SY5Y cell line genome-edited via CRISPR/Cas9 technology to introduce the mutation c.892dupA.

We found that both hNSCs silenced for *SPART* and SH-SY5Y cells carrying the *SPART* loss-of-function mutation presented significant neurite outgrowth/length coupled to extensive cell loss (Fig. 2), in line with the data observed in animal models (14). Gene expression analysis in zebrafish embryos identified high expression of the *SPART* homologous (*spg20b*) through the initial phases, during cleavage and blastula periods - 0.75-5 hours post fertilization (Supplementary Fig. 2A). In adult zebrafish brain, *spg20b* expression was 18 times higher than in heart and liver tissues (Supplementary Fig. 2B).

We observed significant changes in the mitochondrial network and significant mitochondrial fragmentation in absence of Spartin (Fig. 4D-E) with possible detrimental effects on dendrites and axons during synaptic transmission (52, 53).

In concordance, we observed that *SPART*^{dup892A} cells presented a mitochondrial impaired respiration with decreased ATP synthesis specifically due to a decreased Complex I activity (Fig. 5), with a reduced mitochondrial membrane potential and increased oxidative stress (with concomitant decreased expression of ROS detoxifying enzymes; Fig. 7). These data demonstrated that Spartin depletion led to mitochondrial Complex I deficiency. We propose that the mitochondrial impairments found in *SPART*^{dup892A} cell possibly contribute to neurodegeneration (Fig. 8A, B). Perturbations of mitochondrial dynamics or energetic imbalances underpin many neurodegenerative disorders, often with overlapping clinical features such as HSP, Alzheimer's disease, Parkinson's disease, Amyotrophic Lateral Sclerosis and Huntington's disease (54). All neuronal cellular processes are energy demanding and require significantly active mitochondria. Moreover, neurons with long axons, such as peripheral sensory neurons and motor neurons, are more susceptible to neurodegeneration, since they are more sensitive to mitochondrial defects (55).

It is intriguing to note that another form of HSP is due to mutations in spastic-paraplegia-7 gene (*SPG7*), encoding for Paraplegin, a protein forming large complexes in the inner membrane of mitochondria (56, 57). Loss-of-function mutations in *SPG7* lead to a defective Complex I assembly and consequent defective respiratory chain activity (58). Like Paraplegin, Spartin also interacts with GRP75 (Fig. 8A), a member of mitochondrial complex for the import of nuclear-encoded proteins into the mitochondria (37). We hypothesize a role for Spartin in assembly or stability of Complex I, similar to what described for Paraplegin (58). In line with this hypothesis, the increased levels of GRP75 in *SPART* mutant cells might indicate a compensatory effect for Spartin absence (Figure 7F).

In addition to mitochondrial defects, mutant cells presented also specific metabolite imbalances. We identified for the first time an excess of pyruvate in the context of Troyer syndrome (Fig. 6C). Pyruvate is directed into mitochondria through the mitochondrial pyruvate carrier (MPC) located in the mitochondrial inner membrane (MIM). Here, pyruvate functions as fuel input for the citric acid cycle and for mitochondrial ATP generation. Disruption in pyruvate metabolism affects tissues with high demand for ATP. The nervous system is particularly vulnerable because of its high demand of carbohydrate metabolism for ATP generation (59). A previous study in yeast indicated a protective effect of Spartin overexpression on PDH activity, a key enzyme of glucose metabolism that converts pyruvate into acetylCoenzyme A (AcCoA) (19). Our study in a human neuronal cell model identified an increased pyruvate excretion, possibly underlying an impaired pyruvate metabolism, in absence of Spartin, due to the novel human *SPART* mutation (Fig. 8A, B).

Furthermore, Spartin loss was associated with a constitutive phosphorylation (hence activation) of STAT3 (Fig. 6E). STAT3 activation promoted a faster neurite outgrowth (60). Nevertheless, constitutive STAT3 activation was shown to increase glycolysis and decrease oxidative phosphorylation, counteracting PDH activity (35).

PDH inhibition has been also reported in presence of oxidative stress (61-63) and decreased mitochondrial Ca^{2+} levels (64). It is worth noting that the GRP75/VDAC (Voltage-dependent anion channel) complex regulates mitochondrial Ca^{2+} intake from the endoplasmic reticulum, thereby affecting mitochondrial function and intracellular Ca^{2+} homeostasis (37, 65). Consistently, we observed an increase in intracellular Ca^{2+} in *SPART*^{892dupA} cells compared to *SPART*^{wt} cells (Fig. 7G), which was restored to normal levels with the re-expression of Spartin (Fig. 7H). In accordance to Joshi and Bakowska (18), these results suggest that Spartin loss itself affects trafficking and buffering cytosolic and mitochondrial Ca^{2+} via GRP75 interaction.

In summary, through a WES study we were able to assign a diagnosis of Troyer syndrome to otherwise undiagnosed patients and we provided for the first time a thorough assessment of Spartin mutations in a human neuronal cell model. Functional characterization elucidated that the novel mutation in *SPART* led to a profound bioenergetic imbalance, including impaired Complex I activity coupled to increased extracellular pyruvate. Our data support the hypothesis that Spartin coupled with GRP75 might modulate mitochondrial protein import and Ca^{2+} levels, maintaining low ROS levels and a normal ATP production (Fig. 8A). Spartin loss determines an energetic failure, due to altered Complex I function, with increased ROS production and altered intracellular Ca^{2+} possibly leading to reduced PDH activity (59). Therefore, pyruvate is not efficiently converted into acetyl-coA (AcCoA) and is accumulated and excreted from *SPART* mutant cells (Fig. 8B).

Hence, we propose that Troyer syndrome due to *SPART* mutations might be considered a mitochondrial disease. We propose that the observed neuronal phenotypes result from defective protein assembly within mitochondria or defective mitochondrial Complex I function, coupled to an excess of pyruvate and ROS production, generating energetic imbalances that have been already connected to several neurodegenerative disorders, as mentioned previously (54). As the expansion of personalized medicine proceeds, with increasing potential for active analyses of genomic data, the early identification of molecular and genetic defects can lead to a better clinical refinement and the possibility of applying timely targeted therapies. Most importantly, it is crucial to carry out the functional characterization of proteins and mutations, to move forward translational work from gene identification.

Acknowledgements

We thank all patients that participated in the study. We thank Dr. A. Astolfi, Ms. S. Di Battista and Ms. M. Cratere for technical help in sequencing analysis and cell culture, Ms. A. Martinelli, and Dr. M. Gostic for help in zebrafish analysis. We thank Prof. J.M. Lucocq for the helpful suggestions and critical revision of the manuscript.

Author contributions

CD, CB, RD, IL, FB, LM, VAB, NR, FB performed the experiments (including NGS analysis, cell model generation and characterization and mitochondrial assessments); CD, RF, TP, AT, EB performed data analysis; AW, EM, DMC, MS carried out patient assessment; CD, MS, SP, EB wrote the manuscript and supervised the study.

Funding

This work was supported by Telethon grant n. GGP15171 to E.B., AIRC grant IG_17069 to M.S., by the Royal Society grant RG110387 to S.P. Moreover, this work was further supported by the travel fellowship from EuFishBioMed (The European Society for Fish Models in Biology and Medicine), S.P. is a Royal Society University Research Fellow. F.B. is supported by a Telethon fellowship. CD is supported by an AIRC fellowship.

Competing interests

The authors report no competing interests.

URL

Exome Aggregation database (ExAc): http:// http://exac.broadinstitute.org/

Genome Aggregation database (gnomAD): http://gnomad.broadinstitute.org/

Eurexpress: http://www.eurexpress.org

Human Protein Atlas: https://www.proteinatlas.org/ENSG00000133104-SPG20

CRISPR design: crispr.mit.edu

References

1. Deciphering Developmental Disorders Study. (2017) Prevalence and architecture of de novo mutations in developmental disorders. *Nature*. **542**, 433–438.

2. Khokha MK, Mitchell LE, and Wallingford JB. (2017) An opportunity to address the genetic causes of birth defects. *Pediatr Res*. **81**, 282–285

3. Alazami AM, Patel N, Shamseldin HE, Anazi S, Al-Dosari MS, Alzahrani F. (2015) Accelerating novel candidate gene discovery in neurogenetic disorders via whole-exome sequencing of prescreened multiplex consanguineous families. *Cell Rep*. **10**, 148–161.

4. Tawamie H, Wohlleber E, Uebe S, Schmäl C, Nöthen MM, Abou Jamra R. (2015) Recurrent null mutation in *SPG20* leads to Troyer syndrome. *Mol Cell Probes*. **29**, 315–318.

5. Manzini MC, Rajab A, Maynard TM, Mochida GH, MD, Tan WH, Nasir R, MD, Hill RS, Gleason D, Saffar MA, Partlow JN, Barry BJ, Vernon M, LaMantia AS, Walsh CA. (2010) Developmental and Degenerative Features in a Complicated Spastic Paraplegia. *Ann Neurol*. **4**, 516–525.

6. Patel H, Cross H, Proukakis C, Hershberger R, Bork P, Ciccarelli FD, Patton MA, McKusick VA, Crosby AH. (2002) *SPG20* is mutated in Troyer syndrome, a hereditary spastic paraplegia. *Nat Genet*. **4**, 347-8.

7. Bakowska JC, Jenkins R, Pendleton J, Blackstone C. (2005) The Troyer syndrome (SPG20) protein spartin interacts with Eps15. *Biochem Biophys Res Commun*. **4**, 1042-8.

8. Ciccarelli FD, Proukakis C, Patel H, Cross H, Azam S, Patton MA, Bork P, Crosby AH. (2003) The identification of a conserved domain in both spartin and spastin, mutated in hereditary spastic paraplegia. *Genomics*. **4**, 437-41.

9. Diez-Roux G, Banfi S, Sultan M, Geffers L, Anand S, Rozado D et al. (2011) A high-resolution anatomical atlas of the transcriptome in the mouse embryo. *PLoS Biol*. **1**, e1000582.

10. Renvoisé B, Parker RL, Yang D, Bakowska JC, Hurley JH, Blackstone C. (2010) SPG20 protein spartin is recruited to midbodies by ESCRT-III protein Ist1 and participates in cytokinesis. *Mol Biol Cell*. **19**, 3293-303.

11. Eastman SW, Yassaee M, Bieniasz PD. (2009) A role for ubiquitin ligases and Spartin/SPG20 in lipid droplet turnover. *J Cell Biol*. **6**, 881-94.

12. Tsang HT, Edwards TL, Wang X, Connell JW, Davies RJ, Durrington HJ, O'Kane CJ, Luzio JP, Reid E. (2009) The hereditary spastic paraplegia proteins NIPA1, spastin and spartin are inhibitors of mammalian BMP signaling. *Hum Mol Genet*. **20**, 3805-21.

13. Edwards TL, Clowes VE, Tsang HT, Connell JW, Sanderson CM, Luzio JP, Reid E. (2009) Endogenous spartin (SPG20) is recruited to endosomes and lipid droplets and interacts with the ubiquitin E3 ligases AIP4 and AIP5. *Biochem J*. **1**, 31-9.

14. Bakowska JC, Jupille H, Fatheddin P, Puertollano R, Blackstone C. (2007) Troyer syndrome protein spartin is mono-ubiquitinated and functions in EGF receptor trafficking. *Mol Biol Cell.* **5**, 1683–1692.

15. Renvoisé B, Stadler J, Singh R, Bakowska JC, Blackstone C. (2012) Spg20-/- mice reveal multimodal functions for Troyer syndrome protein spartin in lipid droplet maintenance, cytokinesis and BMP signaling. *Hum Mol Genet*. **16**, 3604-18.

16. Milewska M and Byrne PC. (2015) Different expression levels of spartin cause broad spectrum of cellular consequences in human neuroblastoma cells. *Cell Biol Int*, **9**, 1007-15.

17. Truong T, Karlinski ZA, O'Hara C, Cabe M, Kim H, Bakowska JC. (2015) Oxidative stress in Caenorhabditis elegans: protective effects of spartin. *PLoS One*. **6**, e0130455.

18. Joshi DC and Bakowska JC. (2011) SPG20 Protein Spartin Associates with Cardiolipin via Its Plant-Related Senescence Domain and Regulates Mitochondrial Ca^{2+} Homeostasis. *PLoS One*. **4**, e19290.

19. Ring J, Rockenfeller P, Abraham C, Tadic J, Poglitsch M, Schimmel K, Westermayer J, Schauer S, Achleitner B, Schimpel C, Moitzi B, Rechberger GN, Sigrist SJ, Carmona-Gutierrez D, Kroemer G, Büttner S, Eisenberg T, Madeo F. (2017) Mitochondrial energy metabolism is required for lifespan extension by the spastic paraplegia-associated protein spartin. *Microbial Cell.* **12**, 411–422.

20. Bonora E, Bianco F, Cordeddu L, Bamshad M, Francescatto L, Dowless D, Stanghellini V, Cogliandro RF, Lindberg G, Mungan Z, Cefle K, Ozcelik T, Palanduz S, Ozturk S, Gedikbasi A, Gori A, Pippucci T, Graziano C, Volta U, Caio G, Barbara G, D'Amato M, Seri M, Katsanis N, Romeo G, De Giorgio R. (2015) Mutations in RAD21 Disrupt Regulation of APOB in Patients with Chronic Intestinal Pseudo-obstruction. *Gastroenterology*. **4**, 771–782.

21. Graziano C, Wischmeijer A, Pippucci T, Fusco C, Diquigiovanni C, Nõukas M, Sauk M, Kurg A, Rivieri F, Blau N, Hoffmann GF, Chaubey A, Schwartz CE, Romeo G, Bonora E, Garavelli L, Seri M. (2015) Syndromic intellectual disability: a new phenotype caused by an aromatic amino acid decarboxylase gene (DDC) variant. *Gene*. **2**, 144-8.

22. Hsu PD, Scott DA, Weinstein JA, Ran FA, Konermann S, Agarwala V, Li Y, Fine EJ, Wu X, Shalem O, Cradick TJ, Marraffini LA, Bao G, Zhang F. (2013) DNA targeting specificity of RNA-guided Cas9 nucleases. *Nature Biotechnology*. **9**, 827–832.

23. Perez-Pinera P, Kocak DD, Vockley CM, Adler AF, Kabadi AM, Polstein LR, Thakore PI, Glass KA, Ousterout DG, Leong KW, Guilak F, Crawford GE, Reddy TE, Gersbach CA. (2013) RNA-guided gene activation by CRISPR- Cas9 – based transcription factors. *Nature Methods*. **10**, 973–976.

24. Ran FA, Hsu PD, Wright J, Agarwala V, Scott D & Zhang F. (2013) Genome engineering using the CRISPR-Cas9 system. *Nature Protocols*. **11**, 2281–308.

25. Fanti Z, De-Miguel FF, Martinez-Perez ME. (2008) A method for semiautomatic tracing and morphological measuring of neurite outgrowth from DIC sequences. *Conf Proc IEEE Eng Med Biol Soc*. **2008**:1196-9.

26. Dagda RK, Cherra SJ 3rd, Kulich SM, Tandon A, Park D, Chu CT. (2009) Loss of PINK1 function promotes mitophagy through effects on oxidative stress and mitochondrial fission. *Journal of Biological Chemistry*. **20**, 13843–13855.

27. Giuliani A, Lorenzini L, Alessandri M, Torricella R, Baldassarro VA, Giardino L, Calzà L. (2015) In vitro exposure to very low-level laser modifies expression level of extracellular matrix protein RNAs and mitochondria dynamics in mouse embryonic fibroblasts. *BMC Complement Altern Med.* **24**;15-78.

28. Estabrook RV. (1967) Mitochondrial respiratory control and the polarographic measurement of ADP:O ratios. *Methods in Enzymology. Academic Press*. **10**, 41-47.

29. Jones, DP. (1981) Determination of pyridine dinucleotides in cell extracts by high-performance liquid chromatography. *J Chromatogr*. **225**, 446–449.

30. Kirk K, Gennings C, Hupf JC, Tadesse S, D'Aurelio M, Kawamata H. (2014) Bioenergetic markers in skin fibroblasts of sporadic amyotrophic lateral sclerosis and progressive lateral sclerosis patients. *Ann Neurol.* **4**, 620-4.

31. Frezza C, Zheng L, Tennant DA, Papkovsky DB, Hedley BA, Kalna G, Watson DG, Gottlieb E. (2011) Metabolic profiling of hypoxic cells revealed a catabolic signature required for cell survival. *PLoS One*. **9**, e24411.

32. Kenny PA, Lee GY, Myers CA, Neve RM, Semeiks JR, Spellman PT Lorenz K, Lee EH, Barcellos-Hoff MH, Petersen OW, Gray JW, Bissell MJ. (2007) The morphologies of breast cancer cell lines in three-dimensional assays correlate with their profiles of gene expression. *Mol Oncol*. **1**, 84-96.

33. Lu J, Rashid F, Byrne PC. (2006) The hereditary spastic paraplegia protein spartin localises to mitochondria. *J Neurochem.* **6**, 1908-19.

34. Mishra P and Chan D. (2016) Metabolic regulation of mitochondrial dynamics. *J Cell Biol*. **4**, 379:387.

35. Demaria M, Giorgi C, Lebiedzinska M, Esposito G, D'Angeli L, Bartoli A, Gough DJ, Turkson J, Levy DE, Watson CJ, Wieckowski MR, Provero P, Pinton P, Poli V. (2010) A STAT3-mediated metabolic switch is involved in tumour transformation and STAT3 addiction. *Aging.* **11**, 823-42.

36. Sena LA and Chandel NS. (2012) Physiological roles of mitochondrial reactive oxygen species. *Mol Cell.* **2**, 158-67.

37. Honrath B, Metz I, Bendridi N, Rieusset J, Culmsee C, Dolga AM. (2017) Glucose-regulated protein 75 determines ER–mitochondrial coupling and sensitivity to oxidative stress in neuronal cells. *Cell Death Discov*. **3**, 17076.

38. Milewska M, McRedmond J, Byrne PC. (2009) Identification of novel spartin-interactors shows spartin is a multifunctional protein. *J Neurochem*. **4**, 1022-30.

39. Short PJ, McRae JF, Gallone G, Sifrim A, Won H, Geschwind DH, Wright CF, Firth HV, FitzPatrick DR, Barrett JC, Hurles ME. (2018) De novo mutations in regulatory elements in neurodevelopmental disorders. *Nature*. **7698**, 611-616.

40. Wright CF, McRae JF, Clayton S, Gallone G, Aitken S, FitzGerald TW. Making new genetic diagnoses with old data: iterative reanalysis and reporting from genome-wide data in 1,133 families with developmental disorders. *Genet Med.* **10**, 1216-1223.

41. Vissers LE, Veltman JA. (2015) Standardized phenotyping enhances Mendelian disease gene identification. *Nat Genet.* **11**, 1222-4.

42. Firth HV, Wright CF; DDD Study. (2011) The Deciphering Developmental Disorders (DDD) study. *Dev Med Child Neurol*. **8**, 702-3.

43. Tan TY, Dillon OJ, Stark Z, Schofield D, Alam K, Shrestha R, et al. (2017) Diagnostic impact and cost-effectiveness of Whole-Exome Sequencing for ambulant children with suspected monogenic conditions. *JAMA Pediatr.* **9**, 855-862.

44. Krabbenborg L, Vissers LE, Schieving J, Kleefstra T, Kamsteeg EJ, Veltman JA, Willemsen MA, Van der Burg S. (2016) Understanding the Psychosocial Effects of WES Test Results on Parents of Children with Rare Diseases. *J Genet Couns*. **6**,1207-1214.

45. Stark Z, Tan TY, Chong B, Brett GR, Yap P, Walsh M. (2016) A prospective evaluation of whole-exome sequencing as a first-tier molecular test in infants with suspected monogenic disorders. *Genet Med.* **18**, 1090–1096.

46. Fink JK. (2013) Hereditary spastic paraplegia: clinico-pathologic features and emerging molecular mechanisms. *Acta Neuropathol*. **126**, 307–28.

47. Bizzari S, Hamzeh AR, Nair P, Mohamed M, Saif F, Aithala G, Al-Ali MT, Bastaki F. (2017) Novel SPG20 mutation in an extended family with Troyer syndrome. *Metab Brain Dis.* **6**, 2155-2159.

48. Dardour L, Roelens F, Race V, Souche E, Holvoet M, Devriendt K. (2017) *SPG20* mutation in three siblings with familial hereditary spastic paraplegia. Cold Spring Harb Mol Case Stud. **4**, pii: a001537.

49. Spiegel R, Soiferman D, Shaag A, Shalev S, Elpeleg O, Saada A. (2017) Novel Homozygous Missense Mutation in *SPG20* Gene Results in Troyer Syndrome Associated with Mitochondrial Cytochrome c Oxidase Deficiency. *JIMD Rep.* **33**, 55-60.

50. Butler S, Helbig KL, Alcaraz W, Seaver LH, Hsieh DT, Rohena L. (2016) Three cases of Troyer syndrome in two families of Filipino descent. *Am J Med Genet*. **170**, 1780–1785.

51. Bakowska JC, Wang H, Xin B, Sumner CJ, Blackstone C. (2008) Lack of spartin protein in Troyer syndrome: a loss-of-function disease mechanism? *Arch Neurol.* **4**, 520-4.

52. Court FA, Coleman MP. (2012) Mitochondria as a central sensor for axonal degenerative stimuli. *Trends Neurosci*. **6**, 364-72.

53. Cheng A, Hou Y, Mattson MP. (2010) Mitochondria and neuroplasticity. *ASN Neuro.* **5**, e00045.

54. Johri A and Beal MF. (2012) Mitochondrial dysfunction in neurodegenerative diseases. *J Pharmacol Exp Ther*. **3**, 619-30.

55. Su B, Wang X, Zheng L, Perry G, Smith MA and Zhu X. (2010) Abnormal Mitochondrial Dynamics and Neurodegenerative Diseases. *Biochim Biophys Acta*. **1**, 135–142.

56. Casari G, De Fusco M, Ciarmatori S, Zeviani M, Mora M, Fernandez P, De Michele G, Filla A, Cocozza S, Marconi R, Dürr A, Fontaine B, Ballabio A. (1998) Spastic paraplegia and OXPHOS impairment caused by mutations in paraplegin, a nuclear-encoded mitochondrial metalloprotease. *Cell*. **6**, 973-83.52.

57. Patron M, Sprenger HG, Langer T. (2018) m-AAA proteases, mitochondrial calcium homeostasis and neurodegeneration. *Cell Res*. **3**,296-306.

58. Atorino L, Silvestri L, Koppen M, Cassina L, Ballabio A, Marconi R, Langer T, Casari G. (2003) Loss of m-AAA protease in mitochondria causes complex I deficiency and increased sensitivity to oxidative stress in hereditary spastic paraplegia. *J Cell Biol.* **4**, 777-87.

59. Gray LR, Tompkins SC, Taylor EB. (2014) Regulation of pyruvate metabolism and human disease. *Cell Mol Life Sci*. **14**, 2577-604.

60. Zhou L and Too HP. (2011) Mitochondrial localized STAT3 is involved in NGF induced neurite outgrowth. *PLoS One*. **6**, e21680.54.

61. Tabatabaie T, Potts JD, Floyd RA. (1996) Reactive oxygen species-mediated inactivation of pyruvate dehydrogenase. *Arch Biochem Biophys*. **2**, 290-6.

62. Hurd TR, Collins Y, Abakumova I, Chouchani ET, Baranowski B, Fearnley IM, Prime TA, Murphy MP, James AM. (2012) Inactivation of pyruvate dehydrogenase kinase 2 by mitochondrial reactive oxygen species. *J Biol Chem*. **42**, 35153-60.

63. Liemburg-Apers DC, Willems PH, Koopman WJ, Grefte S. (2015) Interactions between mitochondrial reactive oxygen species and cellular glucose metabolism. *Arch Toxicol.* **8**, 1209-26.

64. Holness and Sugden. (2003) Regulation of pyruvate dehydrogenase complex activity by reversible phosphorylation. *Biochemical Society Transactions*. **6**, 1143–1151.

65. Szabadkai G, Bianchi K, Varnai P, De Stefani D, Wieckowski MR, Cavagna D, Nagy AI, Balla T, Rizzuto R. (2006) Chaperone-mediated coupling of endoplasmic reticulum and mitochondrial Ca2+ channels. *J Cell Biol*. **175**, 901–911.

Figure Legends

Figure 1. Identification of *SPART* c.892dupA variant. (A) Pedigree of the consanguineous family and electropherograms of the sequences in family members showing the co-segregation of the change with the spastic paraplegia phenotype. The two sibs are homozygous for the mutation, whereas both parents are heterozygous carriers. **(B)** Representative images of patient's skeletal defects. Hand X-ray showed a delayed bone age of 1 year at 2 years of chronological age and of 2.5 years at 5.5 years of chronological age. **(C)** Generation of *SPART* c.892dupA knock-in SH-SY5Y cell line. Electropherogram of the SH-SY5Y clone sequence carrying the mutation c.892dupA in *SPART* gene and alignment between reference sequence and clone sequence are reported. **(D)** Representative western blot of Spartin protein from *SPART*^{wt} and *SPART*^{892dupA}-SH-SY5Y clone using a specific anti-Spartin antibody) Western confirmed that in *SPART*^{892dupA} cells, the predicted 33KDa mutant Spartin is not produced, whereas in control cells Spartin is normally synthesized with molecular weight of 75-84 KDa. Gamma tubulin was used as endogenous control.

Figure 2. Spartin depletion affects neuronal morphology and cells growth. (A) Representative immunofluorescence images showing *SPART*-silencing in hNSCs. Images showed hNSCs day 0 (not silenced, panels a, d), hNSC scramble day 8 (panels b, e) and hNSC *SPART*-silenced (panels c, f). Panel a-c showed immunostaining for Spartin (red), α-tubulin (green) and DAPI (blue). Panels d-f showed immunostaining for Nestin (green) and DAPI (blue). Images showed an increased neuronal outgrowth in Spartin-depleted hNSCs compared to controls. Scale bars 10 µm. **(B)** Photograms in panel a and b are magnifications showing respectively hNSC *SPART*-silenced and hNSC scramble cells at day 8, immunostained for Nestin (green) and DAPI (blue). Arrows indicate neurite extensions that are absent in scramble-treated cells (arrowheads). Scale bars 50 µm. **(C)** Representative immunofluorescence images of *SPART*^{wt} and *SPART*^{892dupA} SH-SY5H cell lines stained against the neuronal marker PGP9.5. *SPART*^{892dupA} cells showed an increased neuronal morphology compared to *SPART*^{wt} cells. Scale bars 50µm. Merged images (panels d and h) show at

higher magnification the insets of the regions in panels c and g, respectively. Arrowheads in panel d showed the absence of neurites formation in *SPART*^{wt} cells. Arrows in panel h indicate the neurite length generation in *SPART*^{892dupA} cell line. Scale bar 50 µm. **(D)** Representative images of hNSCs after 8 days of *SPART* depletion (panel c, hNSCs si*SPART* Day 8), showing a strong cell loss compared to control cells (panel a and b, hNSCs at day 0 and hNSC scramble-transfected at day 8). Scale bars 10 µm. **(E)** Representative images showing *SPART*^{wt} (control) and *SPART*^{892dupA} cell lines, showing a strong cell loss in *SPART*^{892dupA} cells (panel b) compared to control cells (panel a). Scale bars 50µm.

Figure 3. Morphological characterization of *SPART*^{892dupA} spheroids. **(A)** Morphological evaluation of *SPART*^{wt} and *SPART*^{892dupA}-derived spheroids at 24 and 72 hours (panels a, b representing *SPART*^{wt} spheres and panels d, e representing *SPART* ^{892dupA} spheres). Scale bar 20 µm. Both wild-type and mutant cell lines aggregate at 24 hours and formed spheroids after 72 hours. Panels c and f showed magnification of the indicated regions in panels b and e. *SPART*^{892dupA} spheroids were more rounded (panel f) than control *SPART*^{wt} cells, whereas (panel e) formed more condensed and disorganized aggregates. **(B)** Circularity analysis of spheroids performed with ImageJ at 24 and at 72 hours post seeding. An increased circularity value was observed in *SPART*^{892dupA}-derived spheroids compared to *SPART*^{wt} cells at 24 and 72 hours. Unpaired t-test with Welch's correction was performed. ****p<0.0001, ***p<0.0001, mean ± SEM. **(C)** According to the classification of morphological groups of 3D cell cultures (Kenny et al., 2007). *SPART*^{wt}-derived spheroids meet the criteria for "grape-like", whereas *SPART*^{892dupA}-derived spheroids could be classified as "round", characteristic of more differentiated cells. (**D**) Frequency of classification type for *SPART*^{wt} and *SPART*^{892dupA} 3D cell cultures derived from N=46 images for *SPART*^{wt} and n=38 for *SPART*^{892dupA}.

Figure 4. Spartin loss alters mitochondrial morphology and network. (A) Representative z-stack image of mitochondrial network evaluated using mito-GFP probe by live cell imaging. Control cells showed a more diffused distribution of mitochondria within the cytoplasm of cells, also in neurites (left panel, arrows). However, *SPART*^{892dupA} cells showed a notable perinuclear distribution and absence of mitochondria in neurites (right panel, arrowheads). Scale bars 50 µm. **(B)** Quantitative assessment of mitochondrial interconnectivity measured via live cell imaging (n=35 live cells measured for each cell line) using ImageJ Mitochondrial Morphology plugin. ****p<0.0001, mean ± SEM. **(C)** Mitochondrial morphology assessment showed decreased mean perimeter and mean area and increased roundness value in *SPART*^{892dupA} vs control cells (*p<0.05, ****p<0.0001, mean ± SEM). **(D)** Representative images of 3D z-stacks and relative IMARIS reconstruction of the mitochondrial network visualized via mito-GFP transfection in *SPART*^{wt} and *SPART*^{892dupA} cells. Scale bars: 10 µm. **(E)** Quantification of mitochondrial network volume represented as the mean GFP-isosurface volume per cell (n=5 pictures per group). A significant decrease in the mitochondrial isosurface volume was observed in *SPART*^{892dupA} cells (*p<0.05, Student's t-test).

Figure 5. Spartin loss alters mitochondrial activity. (A) Oxygen consumption rates analysis in intact cells in *SPART*^{wt} (n=3 independent experiments) and *SPART*^{892dupA} cells (n=3 independent experiments). Respiration was measured in DMEM (basal respiration), in presence of oligomycin A (non-phosphorylating respiration) and in presence of FCCP (uncoupled respiration). Data were normalized on citrate synthase activity. Colour legend: white box= *SPART*^{wt} cells; black box= *SPART*^{892dupA} cells; white dotted box= *SPART*^{wt} cells oligomycin A-treated; black dotted box=*SPART*^{892dupA} cells oligomycin A-treated; white striped box= *SPART*^{wt} cells FCCP-treated cells; black striped box= *SPART*^{892dupA} cells FCCP-treated cells. **p<0.01, mean ± SEM. **(B)** ATP/ADP ratio in cellular extracts from *SPART*^{wt} and *SPART*^{892dupA} cells showing a decreased ATP/ADP ratio in mutant cells. Bars indicate standard errors. **p<0.01, mean ± SEM. **(C-E)**

OXPHOS complex activity measurements. **(C)** Complex I+III activity (NADH-cytochrome c oxidoreductase activity) in cell homogenate from $SPART^{wt}$ (n=3 independent experiments) and $SPART^{892dupA}$ cells (n=3 independent experiments). ****p<0.0001, mean ± SEM. **(D)** Complex I activity (NADH-dehydrogenase) in cell homogenate from wild type (n=3 independent experiments) and mutant SHSY-5Y cells (n=3 independent experiments). Data were normalized on citrate synthase activity (CS). *p<0.05, mean ± SEM. **(E)** Complex II+III activity (succinate-cytochrome c oxidoreductase activity) in cell homogenate from $SPART^{wt}$ (n=3 independent experiments) and $SPART^{892dupA}$ cells (n=3 independent experiments). **(F)** ATP level in cellular extracts from $SPART^{wt}$ and $SPART^{892dupA}$ cells grown for 72 hours in the presence and absence of 200 nM rotenone (n=4 independent experiments) **p<0.01, mean ± SEM. **(G)** Mitochondrial membrane potential measurement assessed with Tetramethylrhodamine (TMRM) probe. The TMRM fluorescence emission was normalized on MitoTracker Green emission, (n=12 independent experiments). ****p<0.0001, mean ± SEM.

Figure 6. Mutant $SPART^{892dupA}$ cells showed an increased NADH level and pyruvate excretion. **(A)** NADH autofluorescence measurement showing an increased level in mutant cells compared to controls. **p<0.01, mean ± SEM. **(B)** Extracellular lactate content determination by HPLC in $SPART^{wt}$ and $SPART^{892dupA}$ cells. The extracellular lactate content in culture cell medium was quantified after 24 hours of cell growth by HPLC analysis. The peak area corresponding to lactate was normalized on cell number. **(C)** Extracellular pyruvate production $SPART^{wt}$ and $SPART^{892dupA}$ cells measured by HPLC analysis after 72 hours of cell growth. The peak area corresponding to pyruvate was normalized on protein content by Bradford assay. *p<0.05, mean ± SEM. **(D)** Representative HPLC chromatograms of extracellular media from $SPART^{wt}$ and $SPART^{892dupA}$ cells. Red line indicates medium from $SPART^{892dupA}$ cells, green line indicates medium only (DMEM high glucose) and blue line indicates medium from $SPART^{wt}$ cells. Vertical red line indicates pyruvate. **(E)** Representative western blot analysis showing the expression of phosphorylated and total

STAT3 in the two cell lines. Gamma tubulin was used as endogenous control. *SPART*^{892dupA} showed an increase of P-STAT3 compared to *SPART*^{wt} cells, indicating an over-activation of STAT3 in mutant cells. Graph showed the relative quantification of western blot.

Figure 7. Spartin loss increases oxidative stress and alters the homeostasis of calcium. (A) Assessment of reactive oxygen species (ROS) production in *SPART*^{wt} (n=35) and *SPART*^{892dupA} (n=35) SH-SY5Y live cells using dichlorofluorescein diacetate (DCFDA) as fluorescent probe. **(B)** Assessment of mitochondrial superoxide production in *SPART*^{wt} (n=35) and *SPART*^{892dupA} (n=35) SHSY-5Y live cells using MitoSOX Red as specific fluorescent probe. Data were normalized on protein content using the Lowry assay. ****p<0.0001, mean ± SEM. **(C)** *CAT*, **(D)** *SOD1* and **(E)** *SOD2* mRNA relative expression in *SPART*^{wt} and *SPART*^{892dupA} cell lines. *p<0.05, **p<0.01, mean ± SEM. **(F)** Representative western blot analysis showing the expression of GRP75 protein and the relative quantification in the two cell lines. Gamma tubulin was used as endogenous control. *SPART*^{892dupA} showed a higher expression of GRP75 compared to *SPART*^{wt} cells. *p<0.05, mean ± SEM. **(G)** Representative confocal microscopy images showing *SPART*^{wt} and *SPART*^{892dupA} cells stained with Fura-2-AM (right panel). Left panel showed quantification of the Ca^{2+}-free Fura-2 AM relative fluorescence. *SPART*^{892dupA} (n=50) cells showed an increase of intracellular Ca^{2+} compared to control cells (n=50). ****p<0.0001, mean ± SEM. **(H)** Representative confocal microscopy images of Fura-2 AM showing *SPART*^{wt} and *SPART*^{892dupA} cells and re-expression of Spartin in mutant cells (right panel). Left panel showed Spartin re-expression evaluated by western blot and the quantification of the intracellular-free Ca^{2+} measuring the Fura-2 AM relative fluorescence in the three samples. Re-expression of Spartin rescued the intracellular Ca^{2+} concentration. ****p<0.0001, Data are reported as the mean ± SEM of at least three independent experiments.

Figure 8. Model of Spartin functions in mitochondrial metabolism. (A) Spartin interacts with GRP75, modulating the import of mitochondrial proteins encoded by the nucleus via the TIM-TOM

complexes into the mitochondria (Milewska *et al*., 2009), allowing a normal ATP production through Krebs's cycle and OXPHOS activity (Complex I-V). **(B)** Spartin loss, as observed in our experimental settings, determines an energetic failure due to an altered Complex I activity, with a decreased ATP production, and a halt in mitochondrial oxidative phosphorylation leading to decreased mitochondrial membrane potential, and increased oxidative stress, due to enhanced production of mitochondrial ROS. Increased oxidative stress/increased ROS are known inhibitors of PDH activity (Gray *et al.*, 2014). Moreover, Spartin loss results in a reduction of mitochondrial Ca^{2+} levels (Joshi and Bakowska, 2011) which could alter the activity of PDH. Accordingly, we observed that pyruvate, which enters in mitochondria through the mitochondrial pyruvate carrier (MPC), was not efficiently converted into acetyl-coA (AcCoA), Krebs's cycle substrate, thus accumulating and excreted from *SPART*^{892dupA} mutant cells. Therefore, we hypothesize that the energetic failure observed in absence of Spartin, probably related to an impaired mitochondrial protein import of the nuclear-encoded subunits, is pivotal in generating the neurodegenerative defects observed in neurons in Troyer syndrome.

Abbreviations: MPC, mitochondrial pyruvate carrier; PDH, pyruvate dehydrogenase; $\Delta\psi$, mitochondrial membrane potential; MOM, mitochondrial outer membrane; MIM, mitochondrial inner membrane; IMS, inter-membrane space; ECM, extracellular matrix. I-V: mitochondrial OXPHOS complexes; TOM, translocase of the outer membrane; IP3R, Inositol trisphosphate receptor, Phosphatidylinositol 3-phosphate; VDAC, Voltage-dependent anion-selective channel.

Figure 1

Figure 1

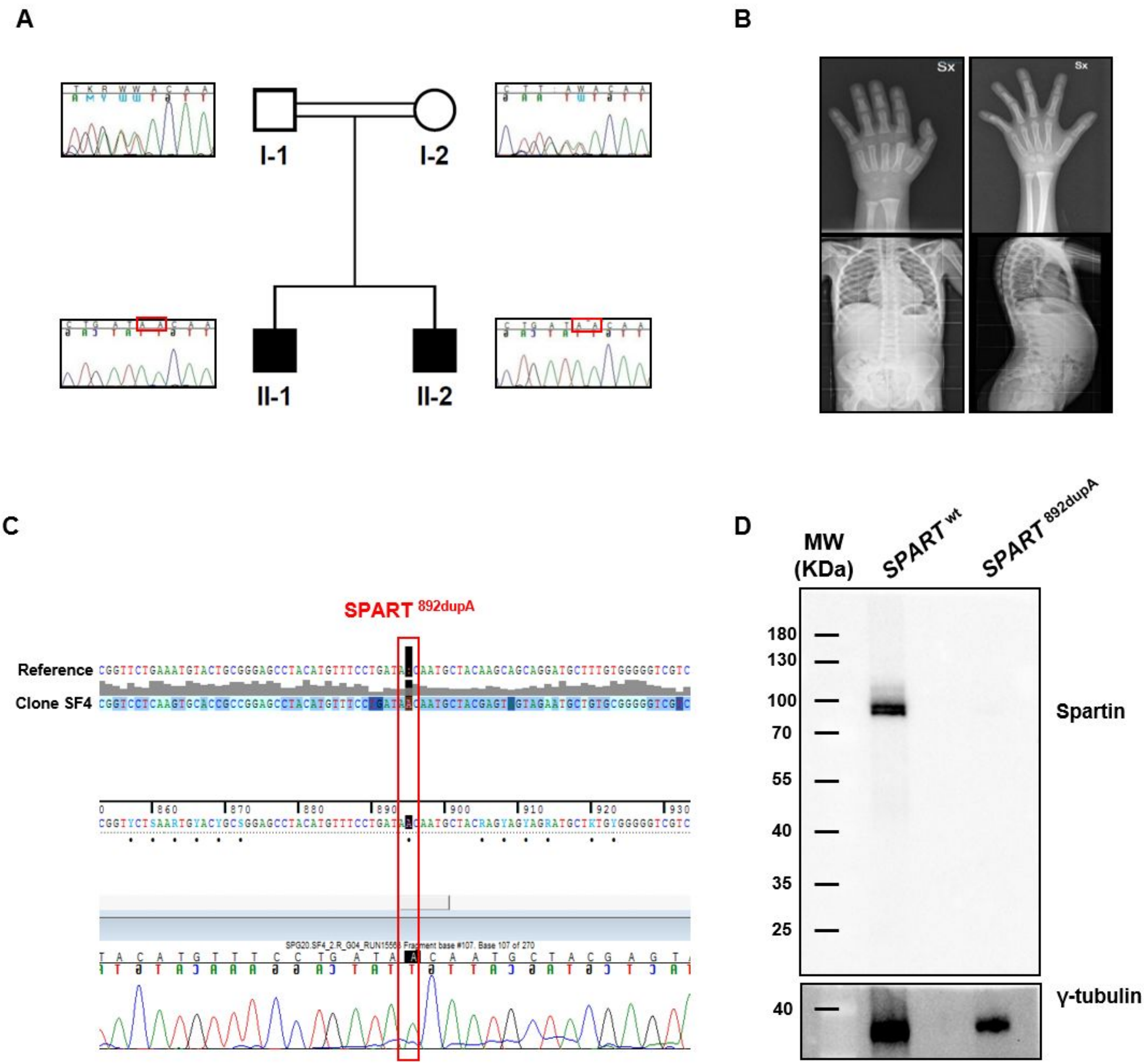

Figure 2

Figure 2

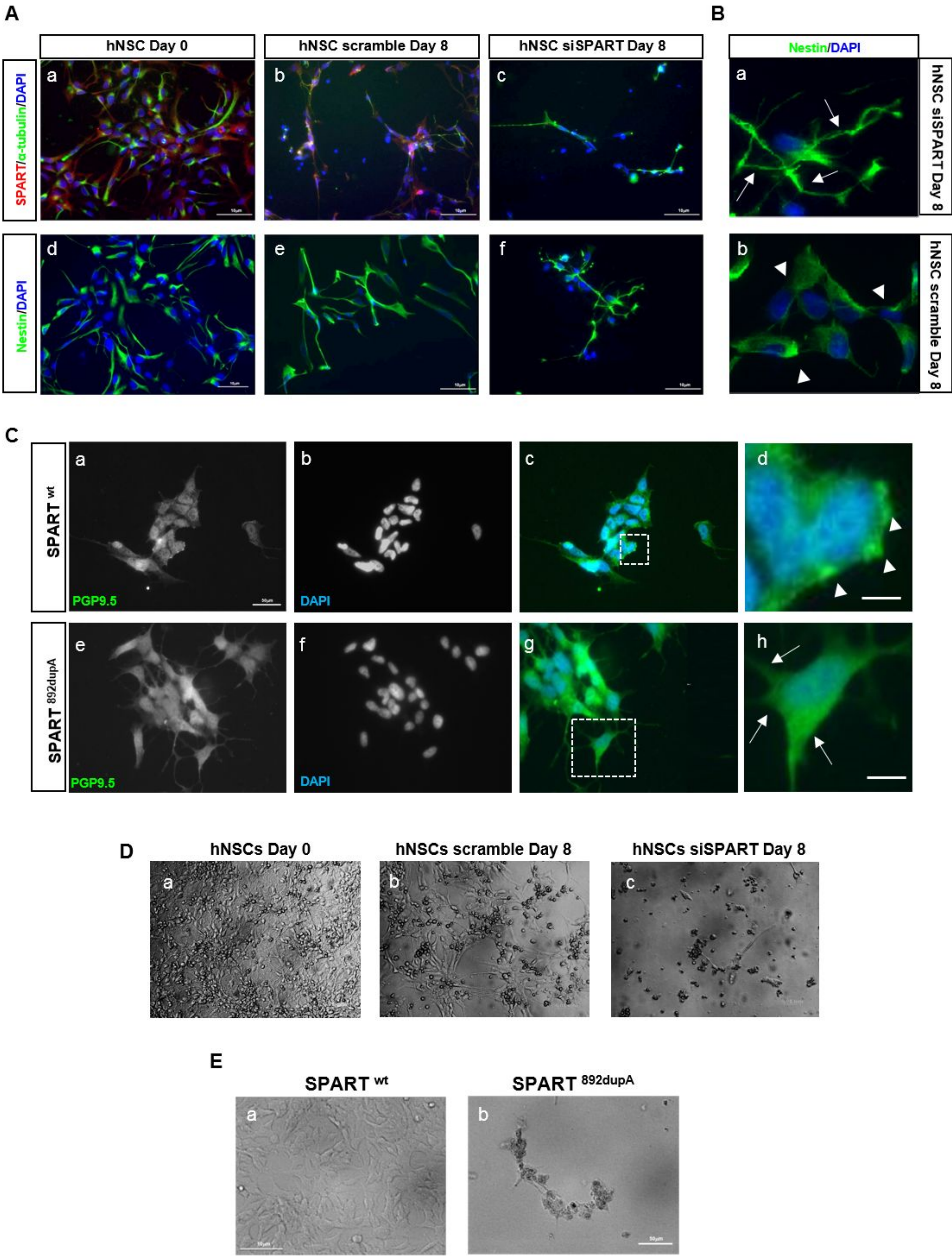

Figure 3

Figure 3

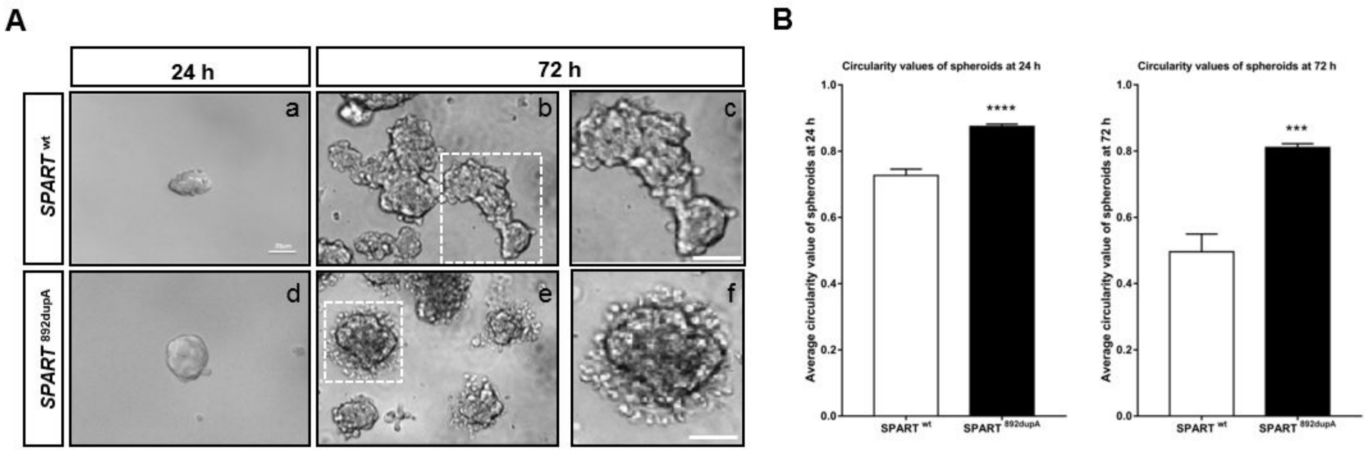

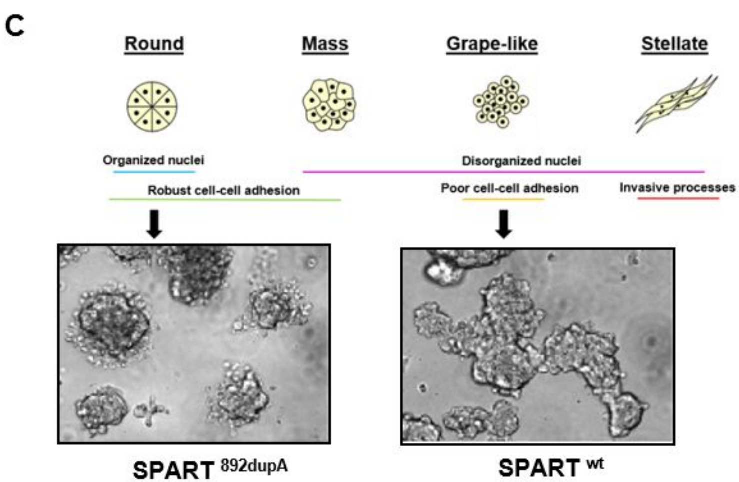

D

Cell line	Round	Grape-like	Fisher's exact test
SPART wt	11	55	P<0.0001
SPART892dupA	88	9	

Figure 3

Figure 3 track changes

A

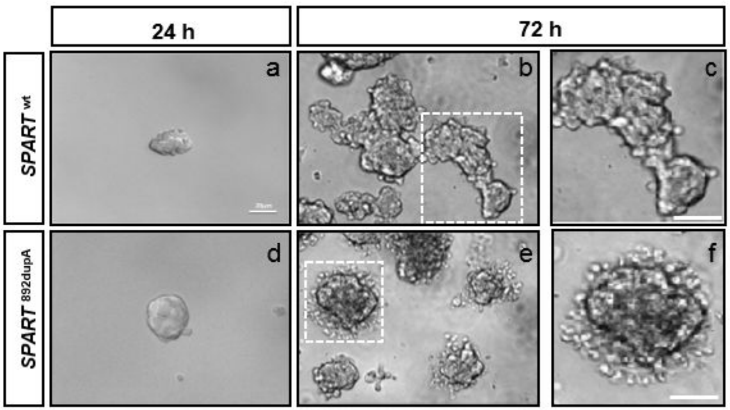

B

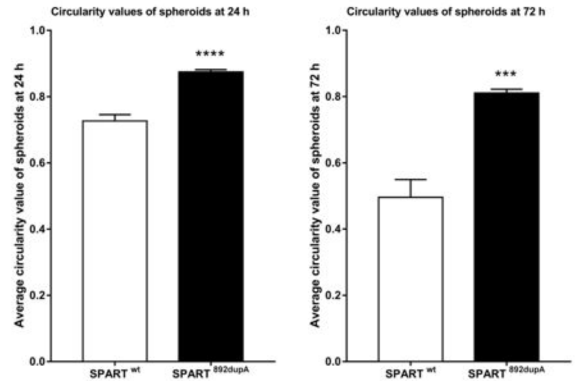

C

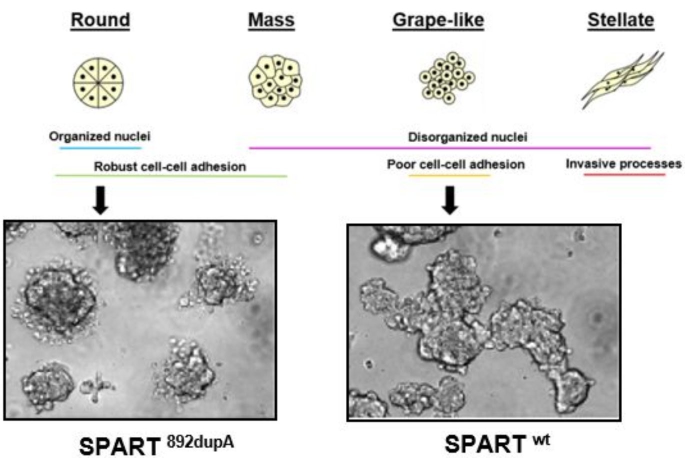

D

Cell line	Round	Grape-like	Fisher's exact test
SPART wt	11	55	P<0.0001
SPART892dupA	88	9	

Figure 4

Figure 4

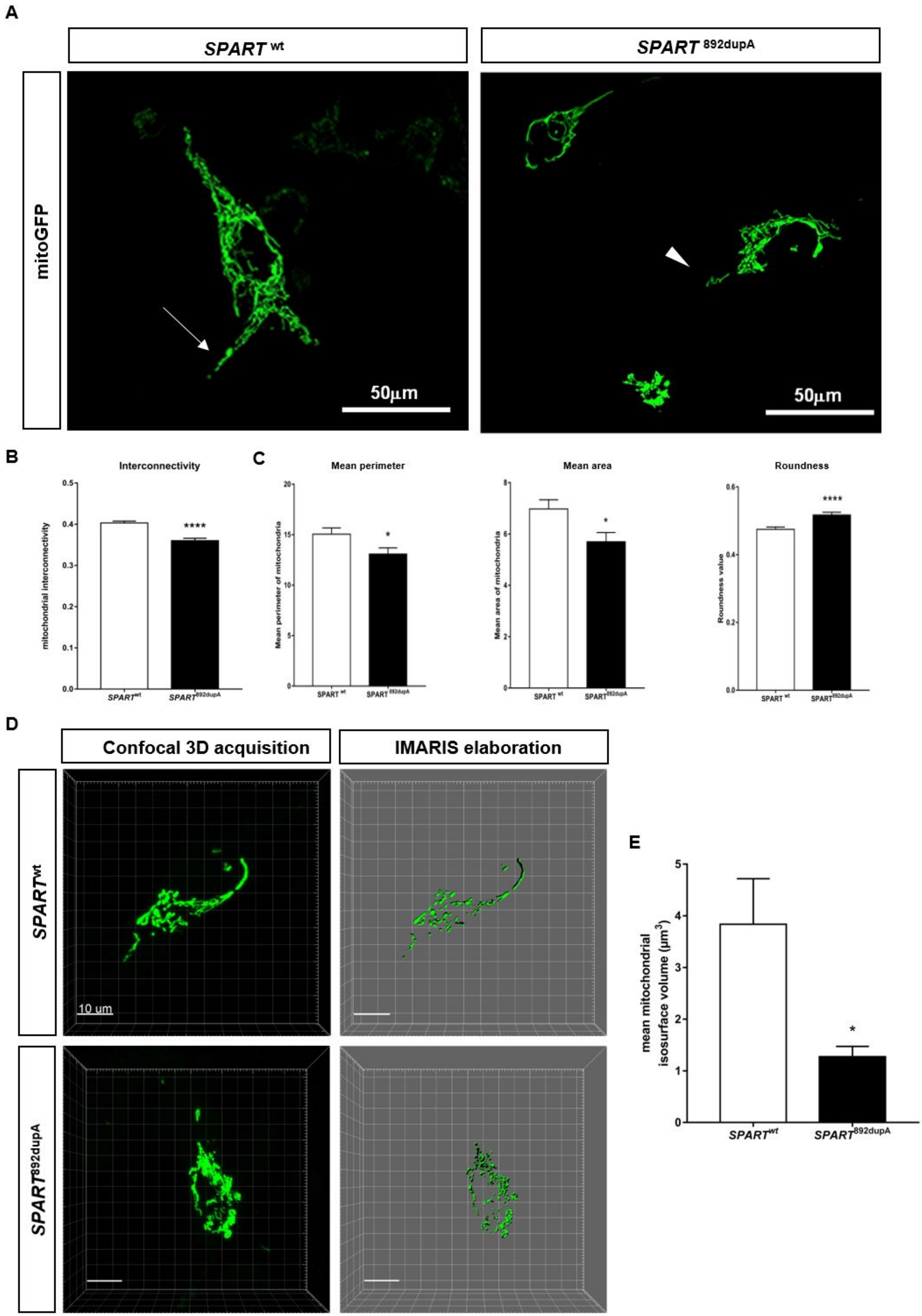

Figure 4

Figure 4 track changes

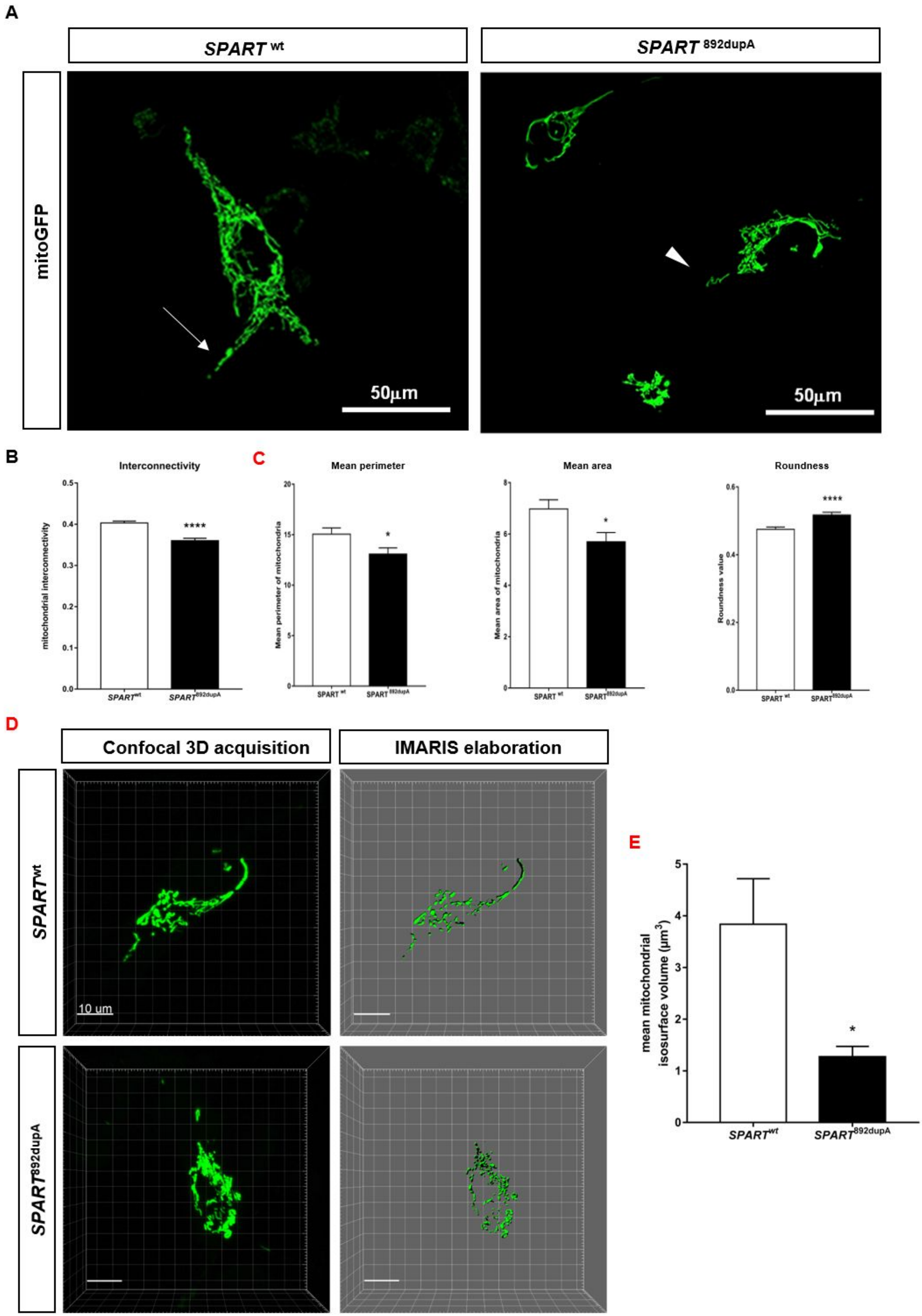

Figure 5

Figure 5

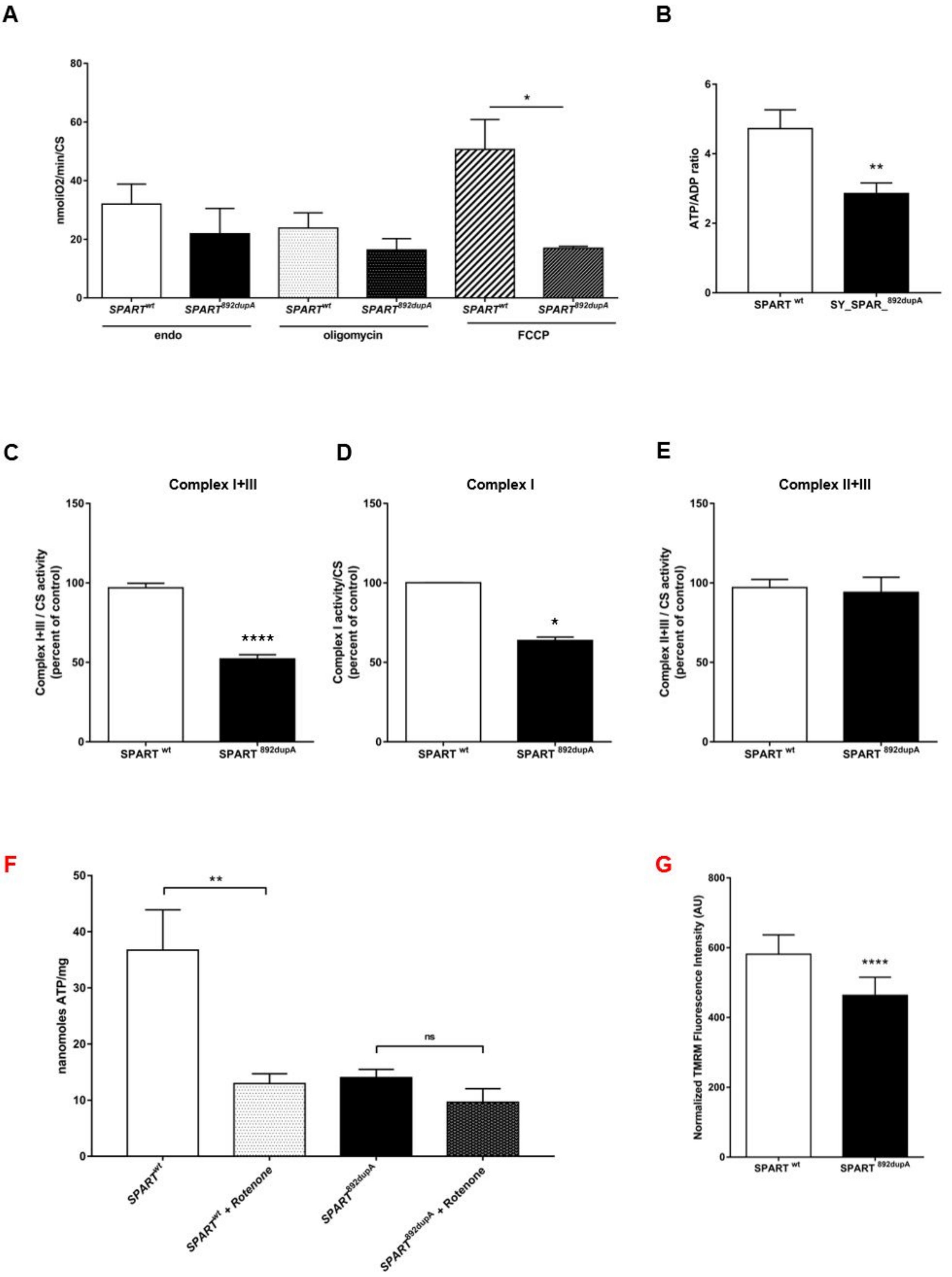

Figure 5

Figure 5 track changes

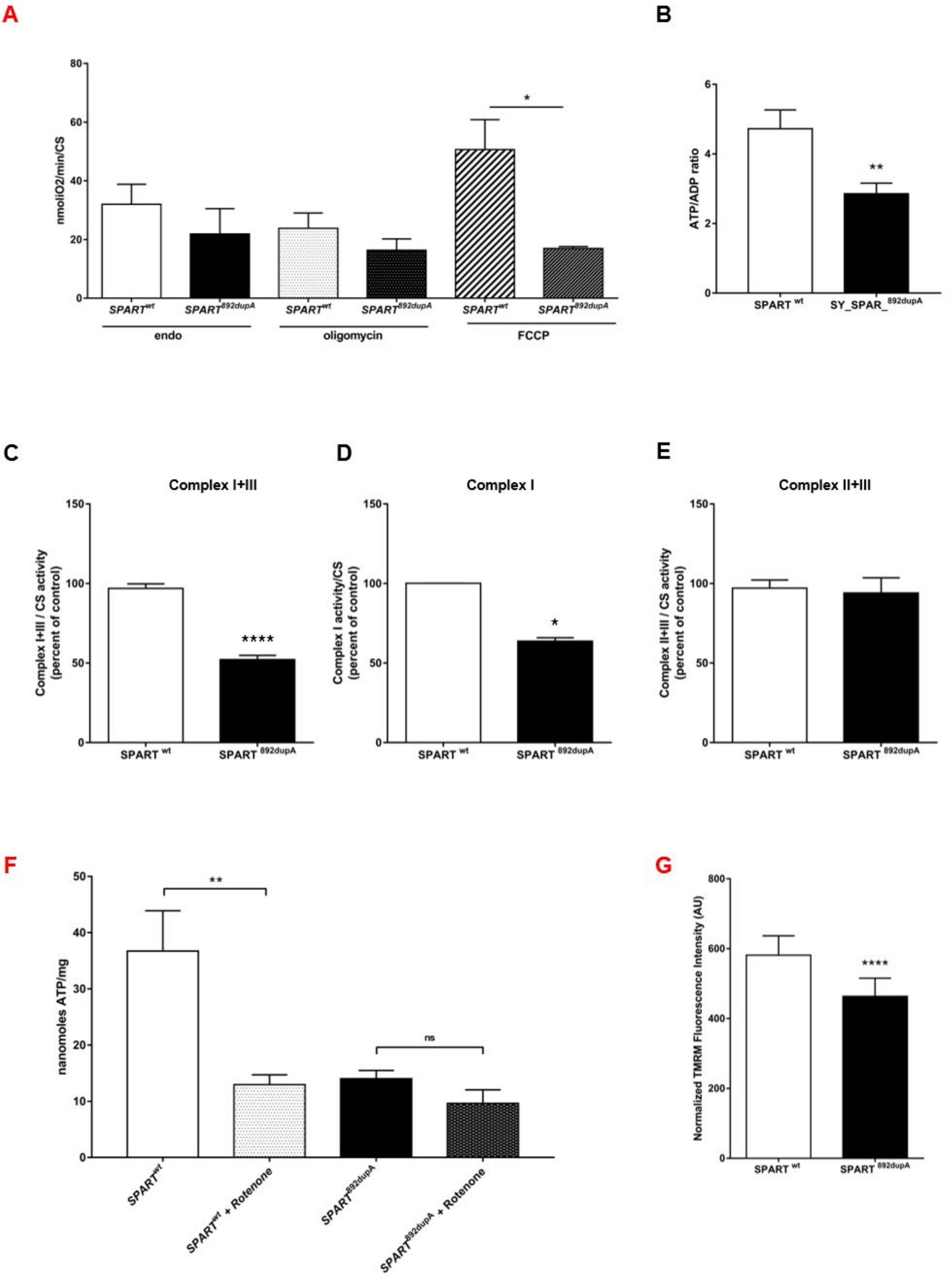

Figure 6

Figure 6

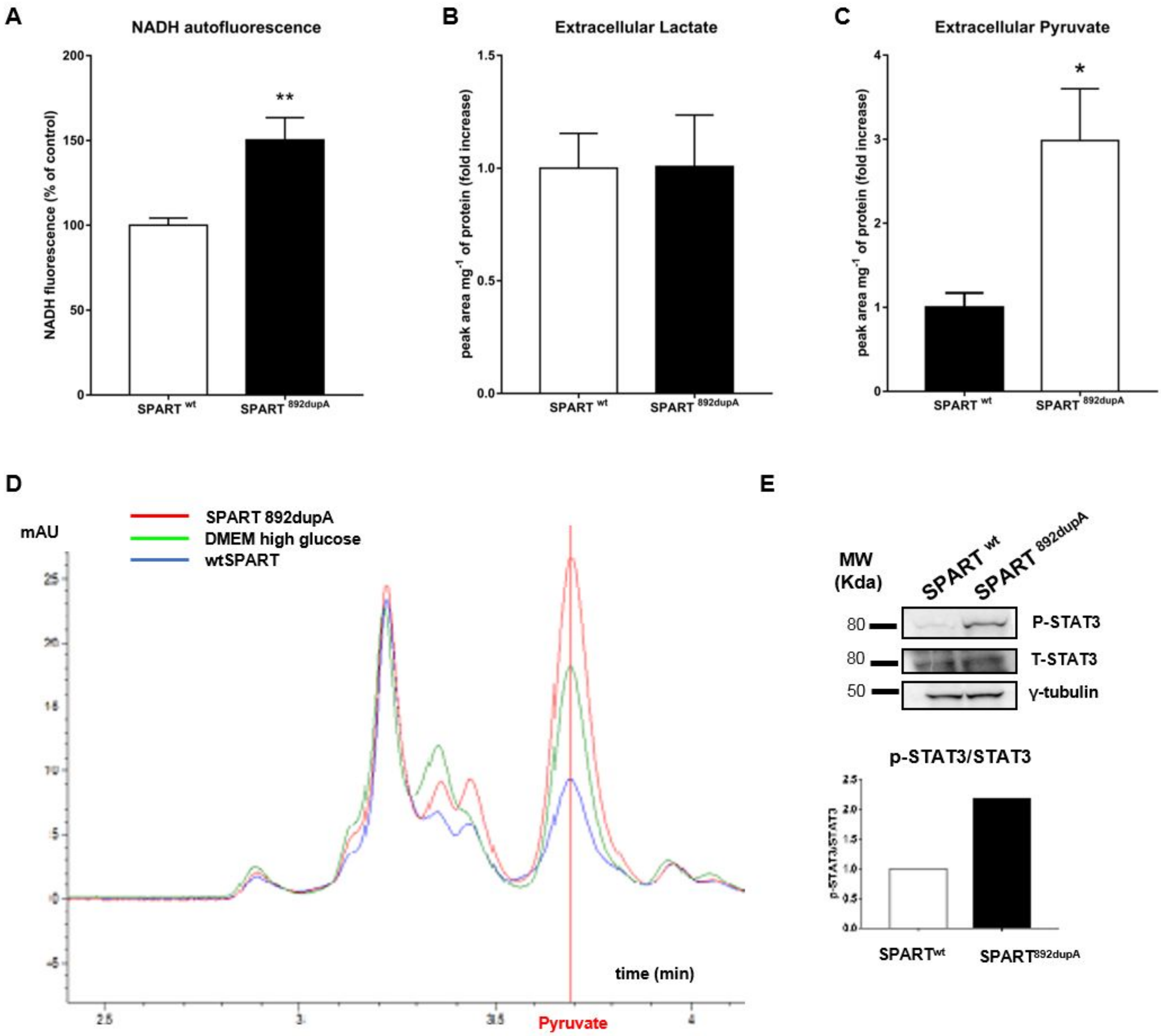

Figure 7

Figure 7

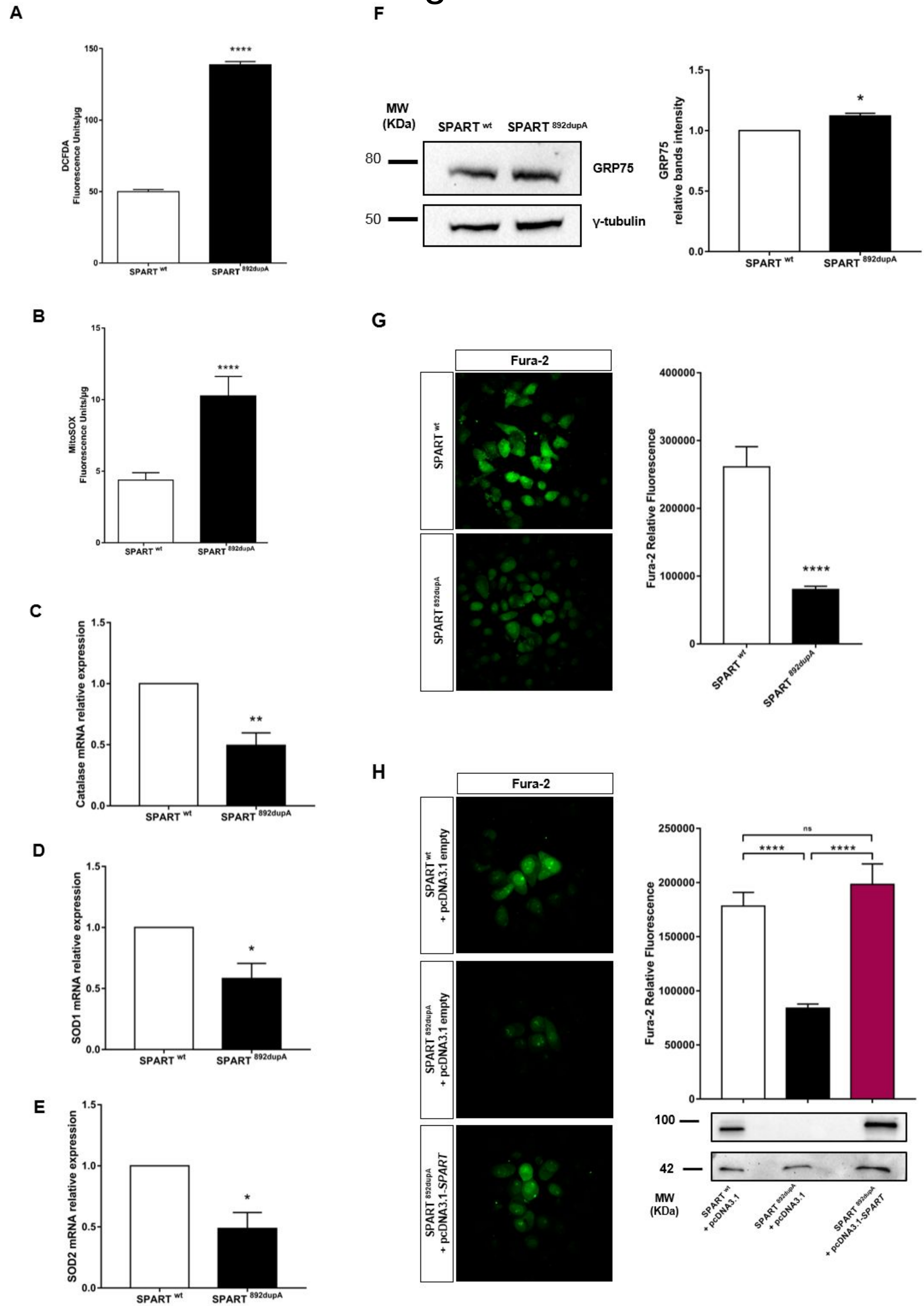

Figure 8

Figure 8

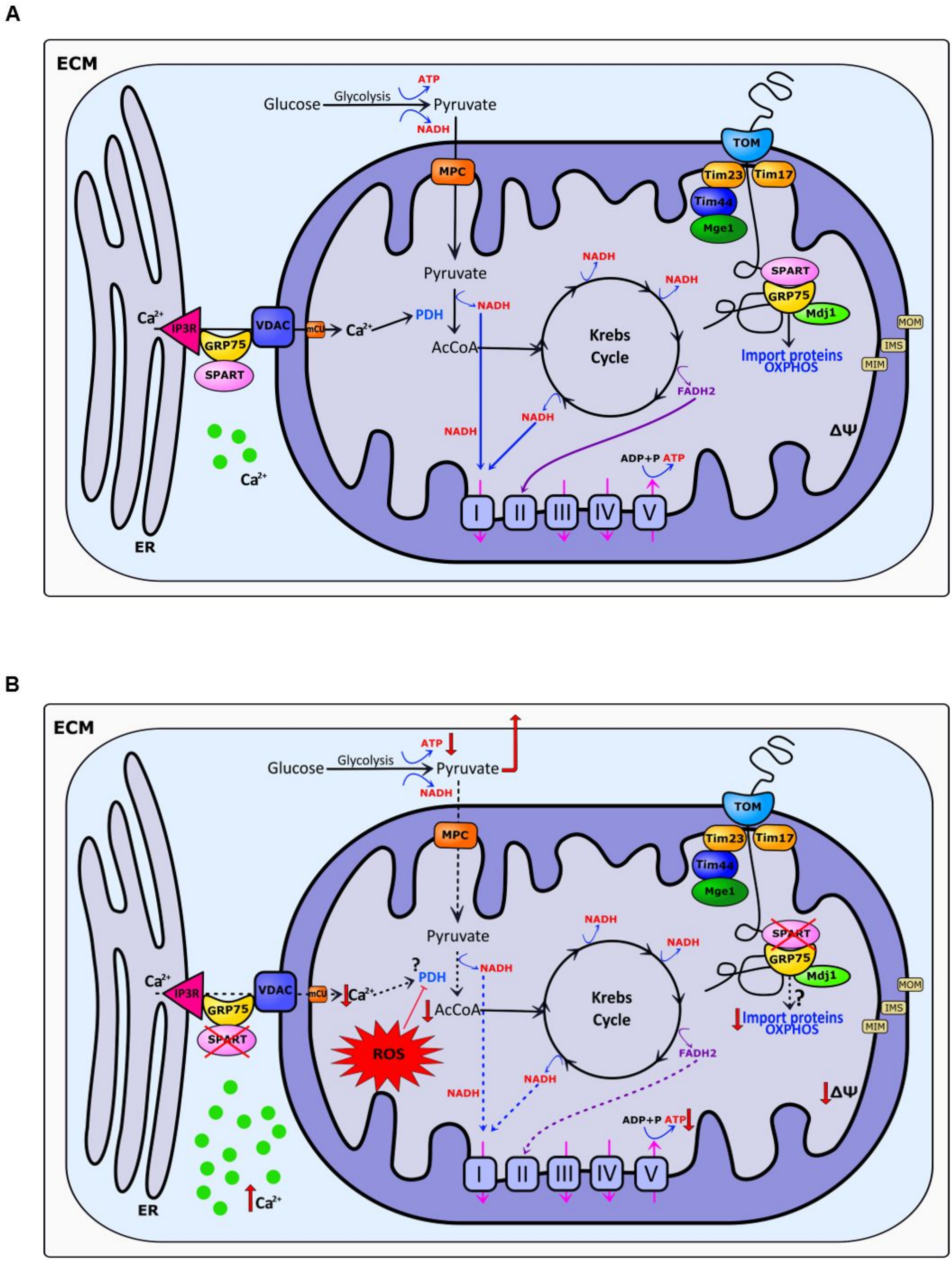

Supplementary Figure 1

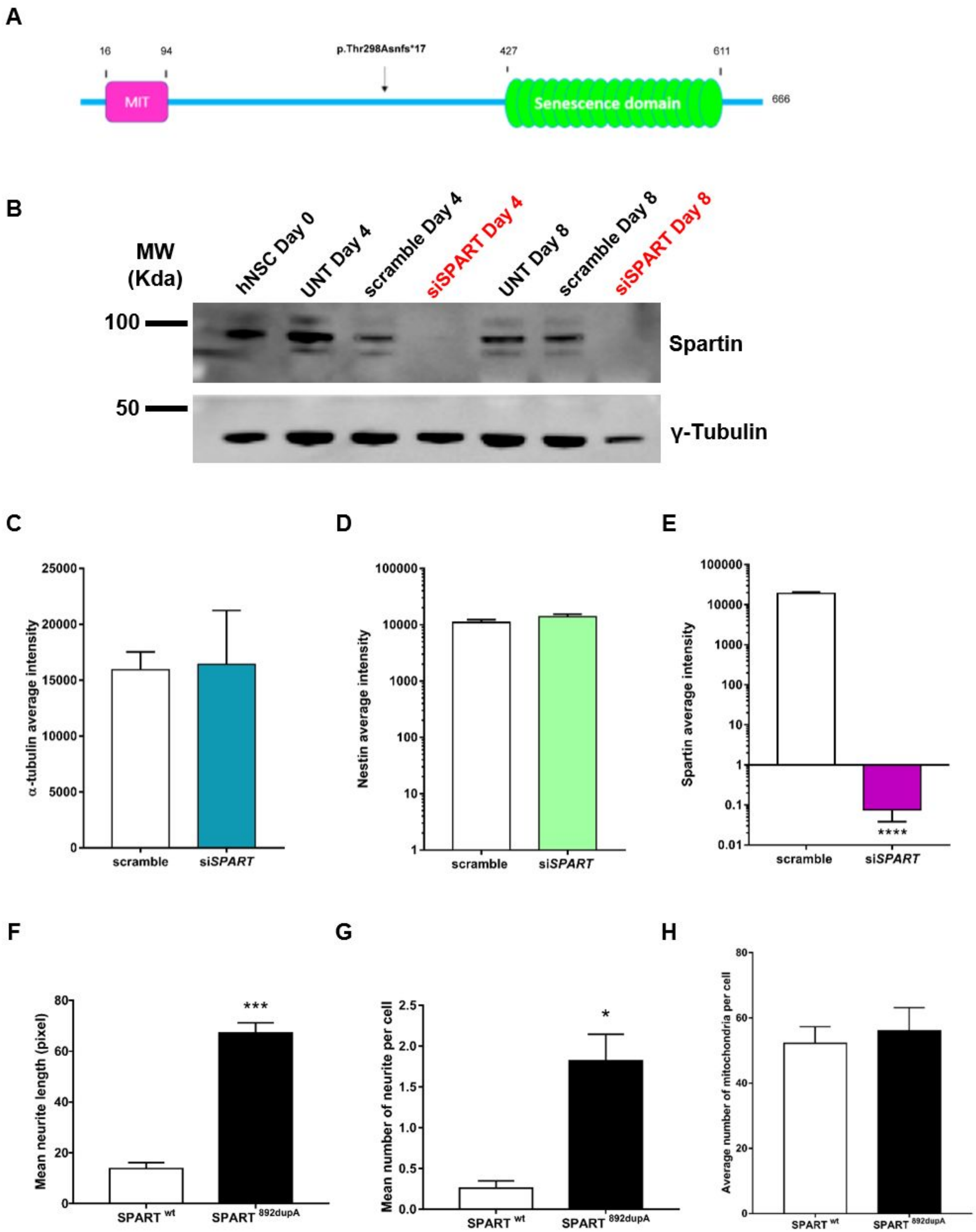

Supplementary Figure 1

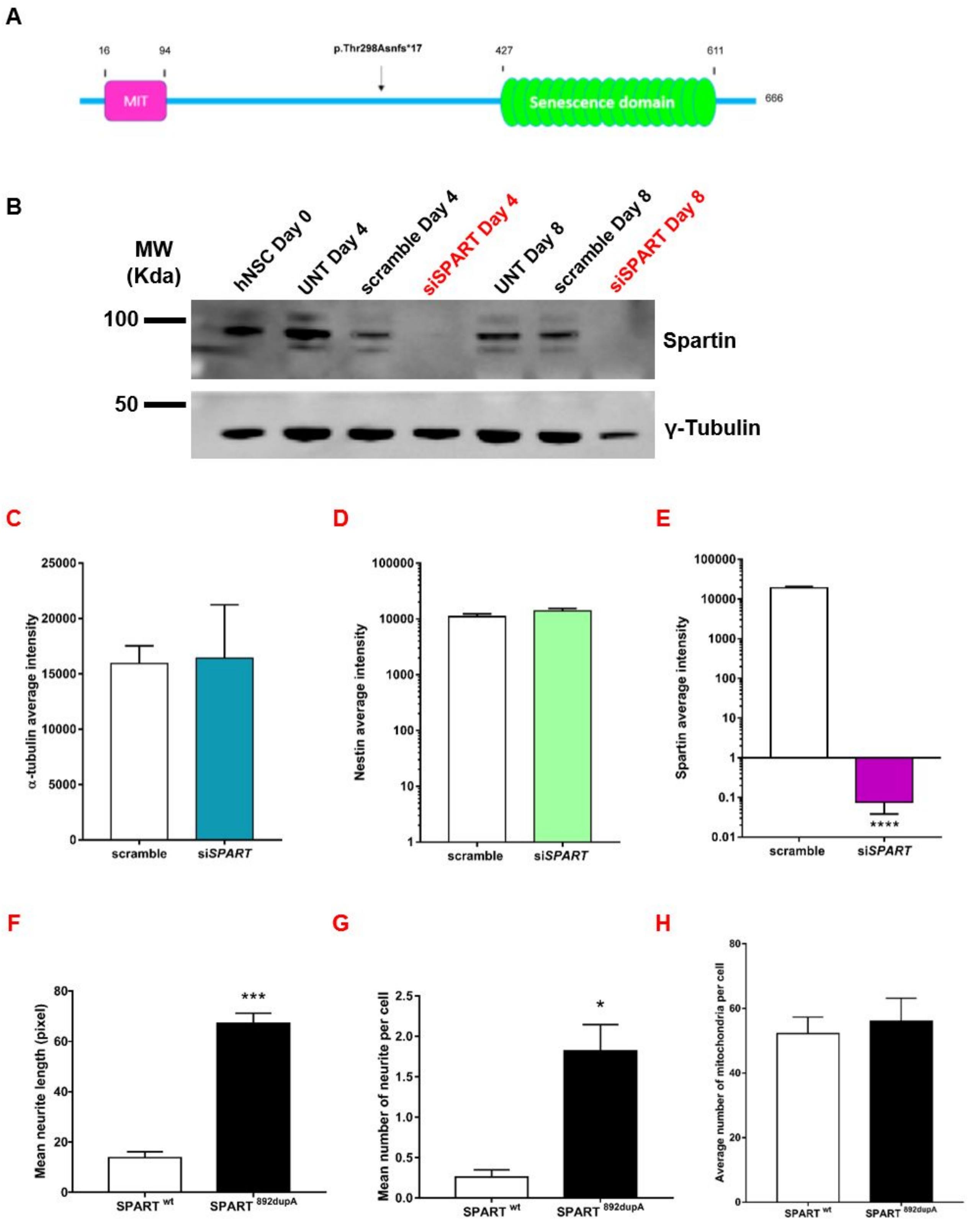

Supplementary Figure 2

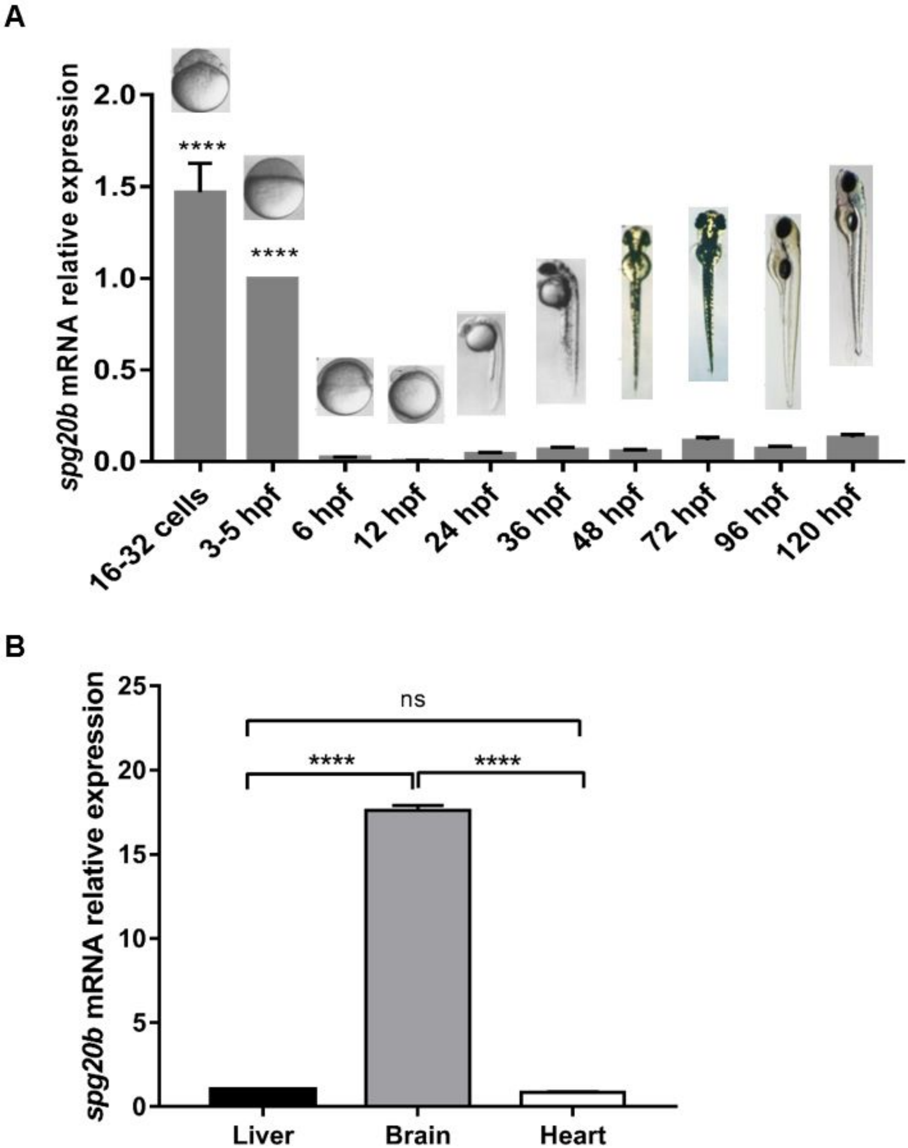

Supplementary Figure 2

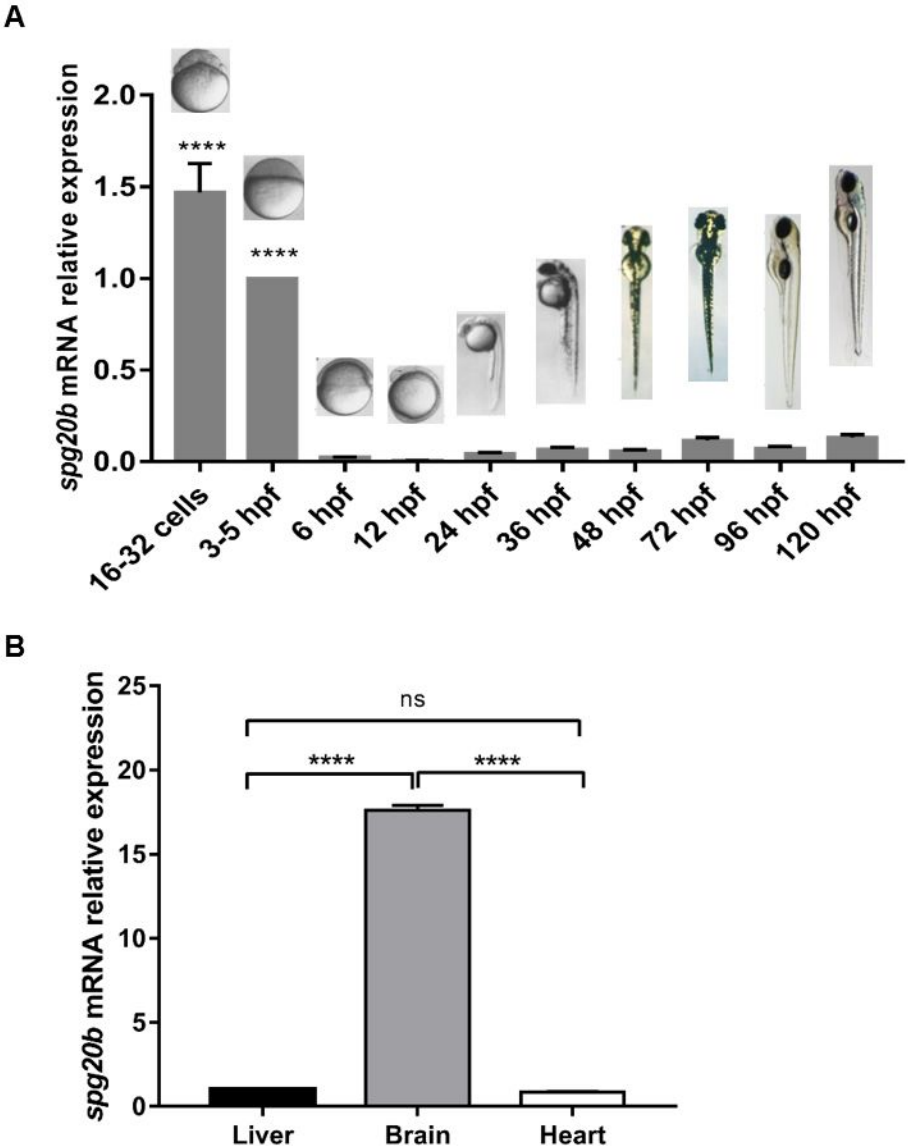

Supplementary Tables

Supplementary Table 1. Primer sequences for Sanger sequencing of WES mutation in *SPART*, gRNA sequences, DNA donor oligo and primers for RT-qPCR are reported.

Primer	Sequence
SPARTx3F	TGTTTCCAACTTTGAAGTGTTTATTT
SPARTx3R	CAATTTCTCTAAAAGCTGAAGTGC
SPART_gRNA-A_1	CACCGCCCGCAGTACATTTCAGAAC
SPART_gRNA-A_2	AAACGTTCTGAAATGTACTGCGGGC
SPART_gRNA-B_1	CACCGACAAGCAGCAGGATGCTTTG
SPART_gRNA-B_2	AAACCAAAGCATCCTGCTGCTTGTC
ssODN_SPART_c.892dupA	GTTTGTGACTGGTTATATCCTCTAGTT
	CCTGATAGATCTCCGGTTCTGAAATGT
	ACTGCGGGAGCCTACATGTTTCCTGAT
	AACAATGCTACAAGCAGCAGGATGCTTT
	GTGGGGGTCGTCCTGTCCTCTGAGTTACC
	AGAGGATGATAGAGAGCTCTTTGAG
CAT_qPCR_F	TAAAGGAGCAGGGGCCTTTGGC
CAT_qPCR_R	GGGAGTCTTCTTTCCAATATGCT
SOD1_qPCR_F	AATACAGCAGGCTGTACCAGT
SOD1_qPCR_R	AGTCTCCAACATGCCTCTCTTC
SOD2_qPCR_F	GTTGGCCAAGGGAGATGTTACA

SOD2_qPCR_R	TTAGGGCTGAGGTTTGTCCA
SOD3_qPCR_F	CGCTACTGTGTTCCTGCC
SOD3_qPCR_R	GTACATGTCTCGGATCCACTC
hActII_qPCR_F	CCTGGCACCCAGCACAAT
hActII_qPCR_R	GGGCCGGACTCGTCATACT
***eef1a1l2* Fw**	TTGAGAAGAAAATCGGTGGTGCTG
***eef1a1l2* Rv**	GGAACGGTGTGATTGAGGGAAATTC
***spg20b* Fw**	CTTTCTCCAGGTTTGTGACTGG
***spg20b* Rv**	ATCATGTCGGGGAACATGTAGA
SPG20_HindIII Fw	GAGAGAAAGCTTATGGAGCAAGAGCCACAAAATATG
SPG20_XhoI Rv	GAGAGACTCGAGTCATTTATCTTTCTTCTTTGCCTCC

Supplementary Table 2. Mutations reported in *SPART* in Troyer syndrome.

References	Mutation	Transcript
Manzini *et al.*, 2010 Tawamie *et al.*, 2015 Butler *et al.*, 2016	c.1110delA (p.Lys369fs*29)	NM_001142294
Patel *et al.*, 2002 Bakowska *et al.*, 2008	c.364_365delAT (p.Met122Valfs*)	NM_001142294
Bizzarri *et al.*, 2017	c.1324G>C (p.Ala442Pro)	NM_001142294
Dardour *et al.*, 2017	c.1369C>T (p.Arg457*)	NM_001142294

present paper (Diquigiovanni *et al.*)	c.892dupA (p.Thr298Asnfs*17)	NM_001142294

Supplementary Figure Legends

Supplementary Figure 1. **Spartin protein analysis in neural cell models. (A)** Representative image of Spartin protein showing the Microtubule Interacting and Trafficking domain (MIT) (aa 16-94) and the senescence domain (aa 427-611). The mutation identified in the two brothers is indicated by an arrow (duplication of nucleotide 892 at amino acid 298 to truncate the 666-amino acid long protein at amino acid 315). **(B)** Representative western blot of Spartin protein after gene silencing in hNSCs. First lane: hNSC lysed at day 0; second lane: untransfected hNSCs lysed at day 4; third lane: hNSCs transfected with scramble siRNAs lysed at day 4; forth lane: hNSCs transfected with siRNAs specific to *SPART* transcripts lysed at day4; fifth lane: untransfected hNSCs lysed at day 8; sixth lane: hNSC transfected with scramble siRNAs lysed at day 8; seventh lane: hNSCs transfected with siRNAs specific to *SPART* transcripts lysed at day 8. The image showed the complete absence of Spartin protein after 4 and 8 days of silencing. Gamma tubulin was used as reference. **(C-E)** Quantitative analysis of alpha-tubulin, nestin and Spartin immunolabeling in cell treated with scramble siRNA and with siRNA specific to *SPART* transcripts. Quantification of the average intensity with background subtraction was performed with ImageJ and at least 10 cells were analysed. Data are represented as mean ± SEM, ****p<0.0001. **(F-G)** Quantitative analysis of neurite length and neurite number respectively. *SPART*^{892dupA} mutant cells (n=20) showed a strong increase in the number of neurites per cell and in their length compared to *SPART*^{wt} (n=20). ***p<0.0001; *p<0.05, mean ± SEM. **(H)** Mitochondrial mass measurement with mito-GFP probe in live-cells. Fluorescence signal was quantified using ImageJ standard tools. Values are reported as mean ± SEM. *p<0.01.

Supplementary Figure 2. Gene expression analysis in zebrafish. (A) Gene expression analysis of *spg20b* gene at different zebrafish developmental stages, spanning from 16–32 cells, up to 120 hours post-fertilization (hpf). A very high *spg20b* expression was identified at the 16–32 cells and 3–5 hpf stages (including cleavage and blastula periods), suggesting an important role for Spartin in these initial developmental phases. Representative optical images of zebrafish embryos/larvae morphology at each development stages are shown. **(B)** Gene expression analysis of *spg20b* gene in zebrafish adult heart, liver and brain tissues. We observed a *spg20b* expression 18 folds times higher in brain compared to liver and heart. ****$p<0.0001$, mean ± SEM.

Supplementary Tables

Supplementary Table 1. Primer sequences for Sanger sequencing of WES mutation in *SPART*, gRNA sequences, DNA donor oligo and primers for RT-qPCR are reported.

Primer	Sequence
SPARTx3F	TGTTTCCAACTTTGAAGTGTTTATTT
SPARTx3R	CAATTTCTCTAAAAGCTGAAGTGC
SPART_gRNA-A_1	CACCGCCCGCAGTACATTTCAGAAC
SPART_gRNA-A_2	AAACGTTCTGAAATGTACTGCGGGC
SPART_gRNA-B_1	CACCGACAAGCAGCAGGATGCTTTG
SPART_gRNA-B_2	AAACCAAAGCATCCTGCTGCTTGTC
ssODN_SPART_c.892dupA	GTTTGTGACTGGTTATATCCTCTAGTT
	CCTGATAGATCTCCGGTTCTGAAATGT
	ACTGCGGGAGCCTACATGTTTCCTGAT
	AACAATGCTACAAGCAGCAGGATGCTTT
	GTGGGGGTCGTCCTGTCCTCTGAGTTACC
	AGAGGATGATAGAGAGCTCTTTGAG
CAT_qPCR_F	TAAAGGAGCAGGGGCCTTTGGC
CAT_qPCR_R	GGGAGTCTTCTTTCCAATATGCT
SOD1_qPCR_F	AATACAGCAGGCTGTACCAGT
SOD1_qPCR_R	AGTCTCCAACATGCCTCTCTTC
SOD2_qPCR_F	GTTGGCCAAGGGAGATGTTACA

SOD2_qPCR_R	TTAGGGCTGAGGTTTGTCCA
SOD3_qPCR_F	CGCTACTGTGTTCCTGCC
SOD3_qPCR_R	GTACATGTCTCGGATCCACTC
hActII_qPCR_F	CCTGGCACCCAGCACAAT
hActII_qPCR_R	GGGCCGGACTCGTCATACT
***eef1a1l2* Fw**	TTGAGAAGAAAATCGGTGGTGCTG
***eef1a1l2* Rv**	GGAACGGTGTGATTGAGGGAAATTC
***spg20b* Fw**	CTTTCTCCAGGTTTGTGACTGG
***spg20b* Rv**	ATCATGTCGGGGAACATGTAGA
SPG20_HindIII Fw	GAGAGAAAGCTTATGGAGCAAGAGCCACAAAATATG
SPG20_XhoI Rv	GAGAGACTCGAGTCATTTATCTTTCTTCTTTGCCTCC

Supplementary Table 2. Mutations reported in *SPART* in Troyer syndrome.

References	Mutation	Transcript
Manzini *et al.*, 2010 Tawamie *et al.*, 2015 Butler *et al.*, 2016	c.1110delA (p.Lys369fs*29)	NM_001142294
Patel *et al.*, 2002 Bakowska *et al.*, 2008	c.364_365delAT (p.Met122Valfs*)	NM_001142294
Bizzarri *et al.*, 2017	c.1324G>C (p.Ala442Pro)	NM_001142294
Dardour *et al.*, 2017	c.1369C>T (p.Arg457*)	NM_001142294

present paper (Diquigiovanni *et al.*)	c.892dupA (p.Thr298Asnfs*17)	NM_001142294

Supplementary Figure Legends

Supplementary Figure 1. **Spartin protein analysis in neural cell models. (A)** Representative image of Spartin protein showing the Microtubule Interacting and Trafficking domain (MIT) (aa 16-94) and the senescence domain (aa 427-611). The mutation identified in the two brothers is indicated by an arrow (duplication of nucleotide 892 at amino acid 298 to truncate the 666-amino acid long protein at amino acid 315). **(B)** Representative western blot of Spartin protein after gene silencing in hNSCs. First lane: hNSC lysed at day 0; second lane: untransfected hNSCs lysed at day 4; third lane: hNSCs transfected with scramble siRNAs lysed at day 4; forth lane: hNSCs transfected with siRNAs specific to *SPART* transcripts lysed at day4; fifth lane: untransfected hNSCs lysed at day 8; sixth lane: hNSC transfected with scramble siRNAs lysed at day 8; seventh lane: hNSCs transfected with siRNAs specific to *SPART* transcripts lysed at day 8. The image showed the complete absence of Spartin protein after 4 and 8 days of silencing. Gamma tubulin was used as reference. **(C-E)** Quantitative analysis of alpha-tubulin, nestin and Spartin immunolabeling in cell treated with scramble siRNA and with siRNA specific to *SPART* transcripts. Quantification of the average intensity with background subtraction was performed with ImageJ and at least 10 cells were analysed. Data are represented as mean ± SEM, ****p<0.0001. **(F-G)** Quantitative analysis of neurite length and neurite number respectively. $SPART^{892dupA}$ mutant cells (n=20) showed a strong increase in the number of neurites per cell and in their length compared to $SPART^{wt}$ (n=20). ***p<0.0001; *p<0.05, mean ± SEM. **(H)** Mitochondrial mass measurement with mito-GFP probe in live-cells. Fluorescence signal was quantified using ImageJ standard tools. Values are reported as mean ± SEM. *p<0.01.

Supplementary Figure 2. Gene expression analysis in zebrafish. (A) Gene expression analysis of *spg20b* gene at different zebrafish developmental stages, spanning from 16–32 cells, up to 120 hours post-fertilization (hpf). A very high *spg20b* expression was identified at the 16–32 cells and 3–5 hpf stages (including cleavage and blastula periods), suggesting an important role for Spartin in these initial developmental phases. Representative optical images of zebrafish embryos/larvae morphology at each development stages are shown. **(B)** Gene expression analysis of *spg20b* gene in zebrafish adult heart, liver and brain tissues. We observed a *spg20b* expression 18 folds times higher in brain compared to liver and heart. ****$p<0.0001$, mean ± SEM.